EXPERIMENTAL AND SIMULATED INVESTIGATION ON THE EFFECT OF CHEMICALLY RETARDED ACID SYSTEMS IN CARBONATES

A Thesis

by

YOON SEOK SOHN

Submitted to the Office of Graduate and Professional Studies of
Texas A&M University
in partial fulfillment of the requirements for the degree of

MASTER OF SCIENCE

Chair of Committee,	Ding Zhu
Committee Members,	A. D. Hill
	Yuefeng Sun
Head of Department,	Duane A. McVay

May 2018

Major Subject: Petroleum Engineering

ABSTRACT

In carbonate acidizing, wormhole development is crucial to the stimulation result. The acid reactivity and injection rate both play important roles in this process. Because the reactivity of HCl with carbonate is high, it is essential to control the diffusion rate and reaction rate in order to generate the most effective wormholes. In a typical interstitial velocity (v_i) to pore volume to breakthrough (PV_{BT}) graph, there exists an optimal point for each curve at which a given amount of acid creates a wormhole that penetrates deepest into the wellbore. In order to improve the efficiency of acidizing and maximize the impact of the stimulation, acid transport and reaction rates need to be balanced. Both physical and chemical means could achieve this goal. Chemical reduction of reactivity employs various chemicals to inhibit the rapid reaction from taking place.

In this study, the wormholing phenomena of three types of novel acid systems were investigated via matrix acidizing coreflood experiments to assess their performance. The results were compared with the performance of conventional 15% HCl. With the experimental data, wormhole length could be calculated with a given volume of acid at their optimal point, as well as reduction in skin and ultimately the impact on production rate. An extensive mathematical modeling of wormhole development was conducted to evaluate their applicability in field scale.

The results show that the optimum PV_{BT} and v_i values of the chemically retarded acids were lower than those of 15% HCl. These novel acids generate wormholes more efficiently at lower v_i compared to 15% HCl. The mathematical modeling also shows that the novel acids performance is better in terms of productivity increase, wormhole penetration length, and skin reduction.

DEDICATION

To Umma and Appa.

ACKNOWLEDGEMENTS

I give thanks to the one and only God for everything.

I would like to thank the chair of committee, Dr. Zhu, for her guidance and support throughout the course of this research, and also the committee members Dr. Hill and Dr. Sun for reviewing the work.

Thanks to the colleagues in petroleum engineering department at Texas A&M University for friendship and great memories together. Special thanks to the members of matrix acidizing group, Jimmy Jin, Robert Shirley, Yuhai Zhou and Haoran Cheng for providing help and insight.

Most importantly, thanks to my parents, Kyung Seon Choi, and Myung Kug Sohn. Mom, thanks for your endless prayers and always believing in me. Dad, thanks for your support and encouragement.

CONTRIBUTORS AND FUNDING SOURCES

This work was supported by a dissertation committee consisting of Professor Zhu and Hill of the Harold Vance Department of Petroleum Engineering and Professor Sun of the Department of Geology and Geophysics.

This graduate study was supported by research assistantship from Texas A&M University and also funded by Acid Stimulation Research Program. The work was conducted for and supported by Fluid Energy Group Ltd.

NOMENCLATURE

β	gravimetric dissolving power
μ	viscosity
ν	stoichiometric constant
ρ	density
ϕ	porosity
χ	volumetric dissolving power
A	surface area
Cs	surface concentration of acid
Cf	fluid phase concentration of acid
D	diameter of wormhole
J_D	productivity index
J_{Ds}	stimulated productivity index
K	permeability
K	dissolution rate constant
L	length
MW	molecular weight
N_{ac}	acid capacity number
N_{Da}	Damkholer number
P	pressure
PV_{BT}	pore volume to break through
$PV_{BT,opt}$	optimum pore volume to break through

Q	flow rate
r_e	reservoir radius
r_w	wellbore radius
r'_w	effective wellbore radius
r_{wh}	wormhole length
s	skin factor
s_a	stimulated skin
s_d	damage skin
Sh	Sherwood number
T	temperature
U	flow rate
v_i	interstitial velocity
$v_{i,opt}$	optimum interstitial velocity
v_{wh}	wormhole velocity
W_{eff}	wormhole efficiency factor
W_B	wormhole B-factor

TABLE OF CONTENTS

Page

LIST OF FIGURES

Page

LIST OF TABLES

Page

1. INTRODUCTION

1.1 Background

About 40% of the entire world’s oil reservoir is within carbonate formation (Jardine et. al 1982). Naturally, carbonate rocks have been studied extensively throughout the history of oil and gas industry. Although the porosity and permeability vary depending on the location of the carbonate formation, its chemical composition allows the formation to be effectively stimulated with acid injection. Matrix acidizing technique has been widely used to stimulate well production by injecting acid into the wellbore. The acid propagates into the formation by creating high permeability channels called wormholes. This improves production rate by lowering skin near the wellbore. Throughout the industry, hydrochloric acid is the most commonly used acid in matrix acidizing for carbonate reservoirs, which could be seen in the acidizing guidelines by Mcleod (1984). For deep damaged wells in carbonates HCl based acid systems are used. Depending on the injection rate, the efficacy of the stimulation varies significantly; there exists an optimum flux at which the acid generates the wormholes most efficiently at a given temperature and pressure (McDuff et al. 2010). This optimum acid flux provides the desirable shape of wormhole and most effectively stimulates the reservoir per unit volume of acid. On a lab scale, linear core flood experiments are performed to assess the optimal flux for different formations and concentrations of acids. The chemical reaction that describes the acid dissolution of carbonate formation is as following:

$CaCO_3 + 2HCl \rightarrow CaCl_2 + CO_2 + H_2O$……………………………………..…….…………..….(1.1)

This reaction is irreversible, exothermic, and rapid. The efficacy of acid treatment can be improved if the reaction rate could be controlled so that acid does not get spent so rapidly on the surface of the rock and stays active longer which would enable for more effective wormholes.

There are two major ways this reduction of reactivity is achieved. One way is physically limiting the reactivity by denying the protons from HCl to reach carbonate surface. This could be done with increasing the viscosity of the acid mixture. The commonly used guar gum or synthetic polymer that are used to increase viscosity in fracturing fluids can also be used in acidizing fluids to lower the reactivity (Hoefner et al. 1987). This reduction of reactivity is due to the physical hindering of fluid movement due to high viscosity. However, this method is unsuitable for high temperature reservoirs (above 150˚F) in matrix acidizing treatments (Knox et al. 1964). Another way of physically limiting reactivity is with emulsions. The micro-emulsion of acid droplets in oil is an effective method to reduce the reactivity and can be utilized in matrix acidizing treatments. Not all of the acid in oil emulsion are the same, as the size of the acid droplets is strongly related to the reactivity of the emulsified acid. Because they are thermodynamically stable, emulsified acids can be used in wells with hotter temperatures compared to gelled acids (Hoefner et al. 1987). They achieve somewhat successful results in the field by increasing the production rate up to 75% (Bergstrom et al. 1975). However, even the emulsified acid has higher apparent viscosity which results in higher pumping rates which is economically unfeasible. Furthermore, it cannot be used with many common chemical additives due to the nature of the emulsion which limits the options for production engineers (Knox et al. 1964).

HCl reactivity can also be reduced by chemical means. This is done by chemically inhibiting hydrogen ions (protons) from touching the surface of $CaCO_3$, therefore preventing the dissolution reaction from initiating. The main advantages of chemical retardation is the fact that the viscosity of the acid solution does not increase as they do with emulsified or gelled acids. Also, depending on the molar ratio of the acid to the chemical retarder, the level of retardation can be controlled; this allows the specific design of the acid treatment depending on the environment of the reservoir such as temperature and pressure. As acid becomes more reactive at high temperatures, this type of retardation method can be applicable to reservoirs with wide range of temperatures because of the possibility of controlling the rate of retardation. The main drawbacks of chemical retarders are cost and side reactions that may cause formation damage (Knox et al 1964). Because of the variety of compatible chemicals and their potential, it is of high interest to understand the capabilities of chemically retarded acids in generating wormholes.

1.2 Literature Review

Numerous studies have been conducted for matrix acidizing and wormhole structures. Several work includes studies of retarded acid systems in various formations. Some of the major studies focused on the relationship between interstitial velocity and wormhole penetration length, ultimately obtaining the optimal point at which a given acid volume generates longest wormholes. McDuff et al. (2010) studied the details of wormhole structures depending on the acid flux. Utilizing coreflood experiments, they were able to create the wormhole efficiency curve, in which the optimal flux was determined per acid and rock type. The graph is shown in Figure 1. From this curve, it can be concluded that the interstitial velocity at which the acid travels through the rock is the controlling parameter for wormhole generation. McDuff et al.

concludes that below the optimal rate, the generated wormholes have thicker diameter and do not penetrate deep into the formation, whereas higher-than-optimal interstitial velocity results in ramified wormholes, as shown below in Figure 2.

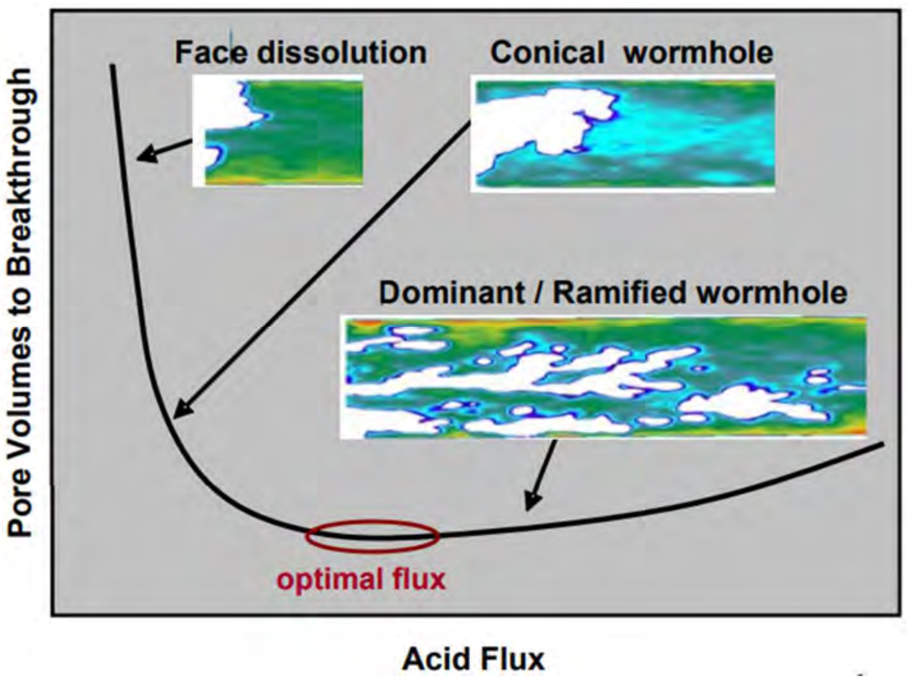

Figure 1. Acid Flux vs. PV_{BT} on Carbonate (reprinted from McDuff et al. 2010)

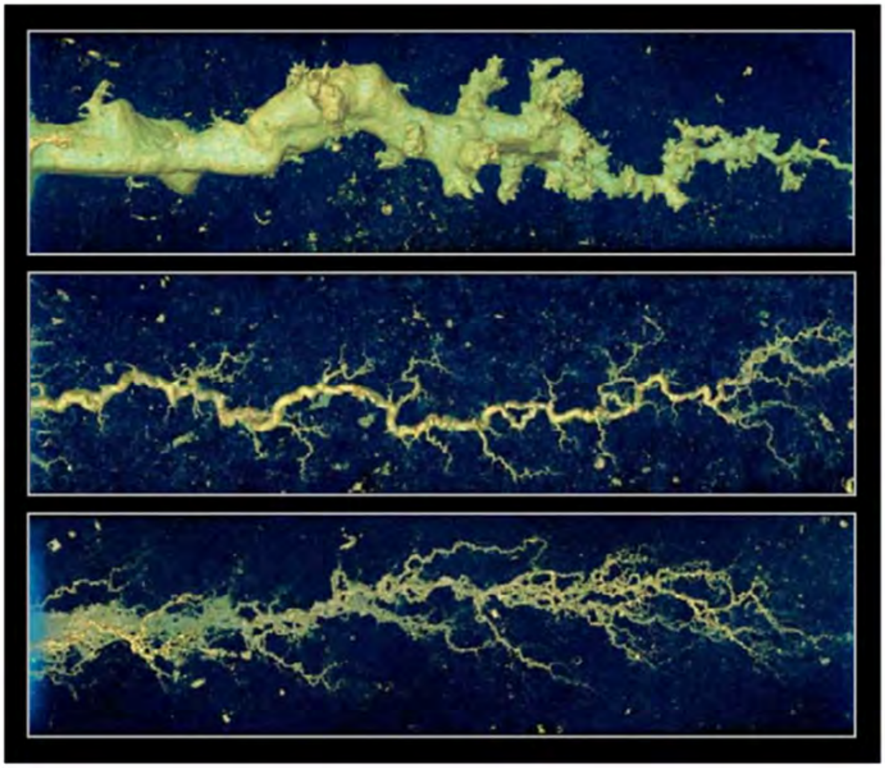

Figure 2. CT scan images of wormholes - low to high acid flux (from top to bottom). (reprinted from McDuff et al. 2010)

Buijse (2000) had carried out mathematical modeling work to understand the differences between reaction-controlled and diffusion-controlled acid dissolution. As it can be seen in Figure 3, the acid penetration depth of the two types of dissolution show large difference. Because the acid dissolution reaction between $CaCO_3$ and HCl is highly diffusion-controlled, it is reasonable to understand that at optimal acid flux, the wormhole development will be the most effective one with highest penetration length.

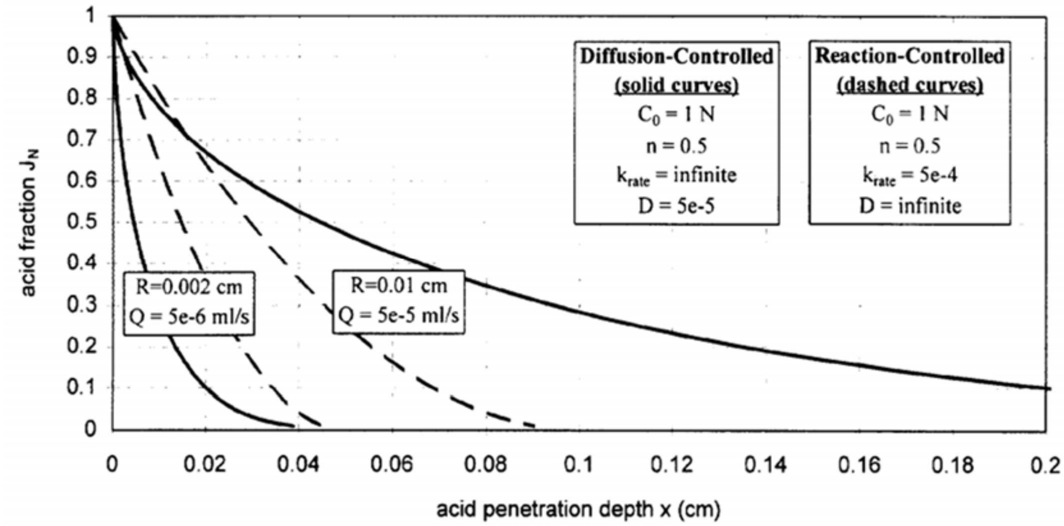

Figure 3. Differences in penetration depth between diffusion-controlled and reaction-controlled acid systems (reprinted from Buijse 2000)

He concluded that the fluid flow contributes significantly in wormhole geometry and development. Also, the fluid loss from wormhole to formation has an effect in the stimulation result as the amount of leak off to formation increases with the wormhole length. The mathematical model developed from core flood tests combines acid spending and tip splitting. This model can provide explanations to the effect of the injection rate and diffusion rate on the wormhole propagation rate.

Fredd and Fogler (1999) also studied the effects of transport and reaction in wormhole generation, but with a variety of acid types. The transport rate and reaction rate were combined together and expressed as the dimensionless Damkohler number,

$$N_{Da} = \frac{\pi * d * L * \kappa}{q} \qquad (1.2)$$

where d is the diameter of wormhole, L is the length of the wormhole, K is the overall dissolution rate constant, and q is the flow rate in the wormhole. This number enables a direct comparison of transport vs. reaction among various acid systems at different flow rates. They then found out the relationship between the PV_{BT} to Damkohler number for various acids and plotted them as can be seen in Figure 4.

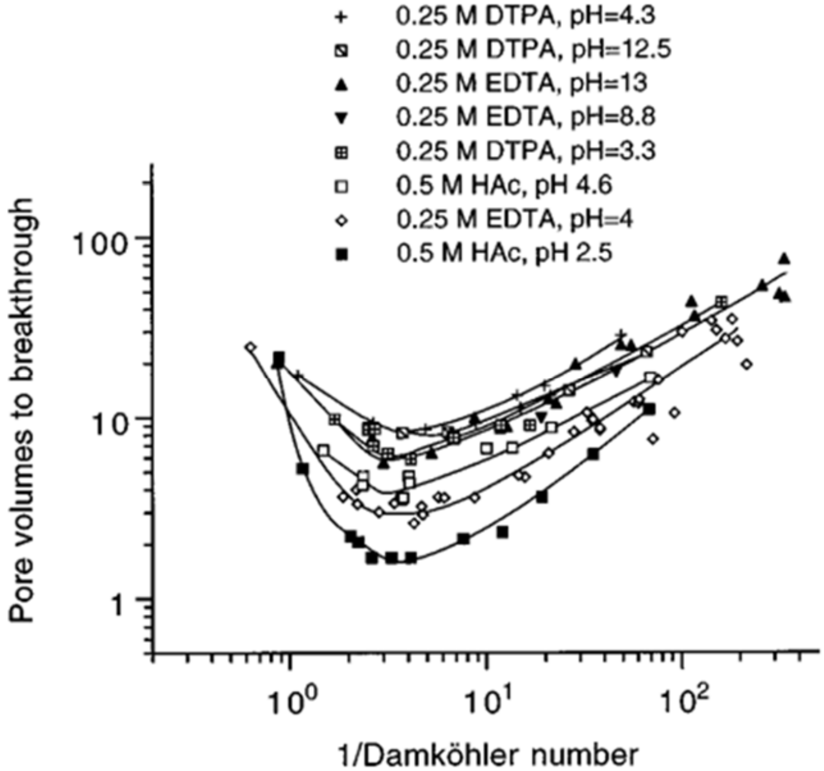

Figure 4. PV_{BT} vs. 1/NDa (reprinted from Fredd and Fogler 1999)

With this result, it is possible to find the optimum Damkohler number at which the most effective wormhole will be generated. This work is significant because it combines reaction and diffusion rate and the optimum can automatically be determined if one or the other rate is known.

Panga et al. expanded the work of Fredd and Fogler by presenting a different model for wormhole formation. Their work incorporates Thiele modulus for pore scale, acid capacity number for each acid and rock, and Damkohler number for core scale. These parameters are defined below:

$$Da = \frac{k_s * a_o * L}{U} \quad (1.3)$$

$$\phi^2 = \frac{2k_s * r_o}{D_m} \quad (1.4)$$

$$N_{ac} = \frac{\alpha * C_o}{\rho_s} \quad (1.5)$$

The effect of reaction regime on optimum injection rate is also studied, and accounted for as this equation:

$$C_s = \frac{C_f}{\left(1 + \frac{\phi^2}{Sh} * r\right)} \quad (1.6)$$

Where Cs is the surface acid concentration, Cf is acid concentration in fluid phase ϕ is porosity Sh is the Sherwood number and r is the dimensionless pore radius (r_p/r_o). They also calculated an effective Damkohler number for the experiments which allows comparison of PV_{BT} curves with different magnitudes of Thiele modulus as seen in Figures 5 and 6. This comprehensive work combines many of the essential parameters in wormhole development. When compared with simulated results, their experimental work shows good agreement in 2D.

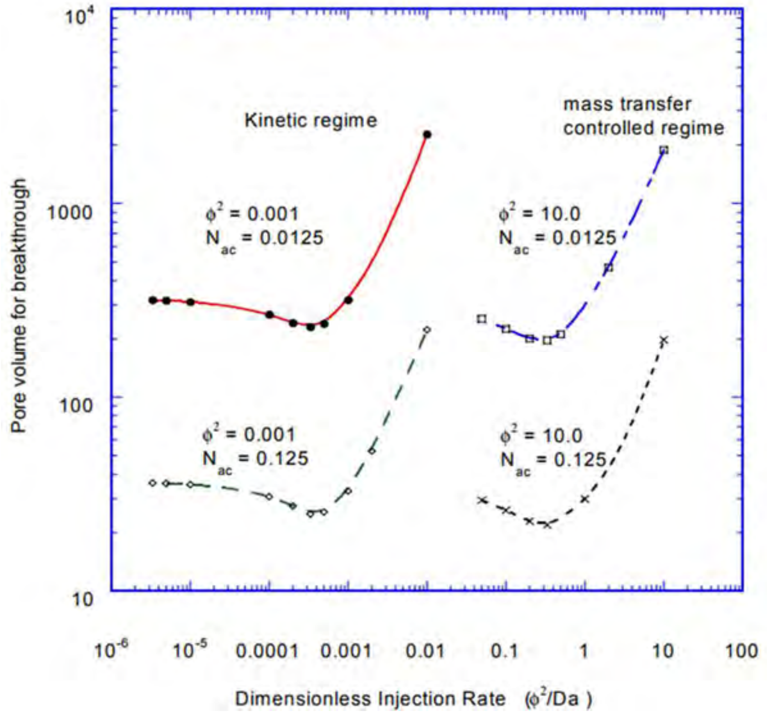

Figure 5. PV_{BT} curve for various Thiele modulus and acid capacity values (reprinted from Panga et al. 2004)

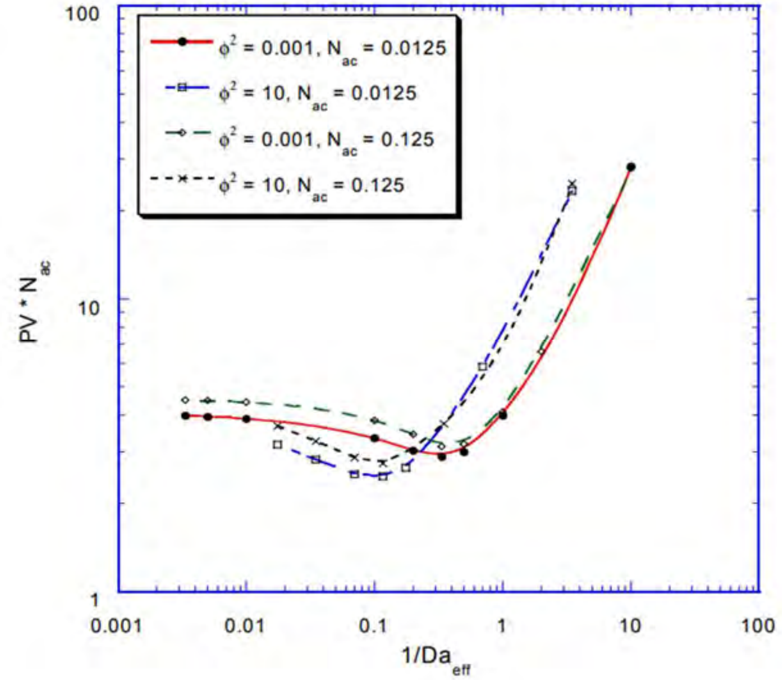

Figure 6. Effective Damkohler number vs. pore volume multiplied by acid capacity (reprinted from Panga et al. 2004)

Buijse et al. in 2005 developed a semi empirical model to calculate wormhole growth which provides equations to calculate many of the crucial factors in the wormholing phenomenon. They categorized common parameters used in modeling the work into four: rock properties (mineralogy, porosity, and permeability), acid concentration and diffusion, acid reaction rate, and acid injection rate. However, there are more factors that play important roles in reality, and they realized those four categories are not specific enough for every possibility. In their work, it was concluded that acid velocity determines the final length of the wormholes, and that the optimum rate exists for the longest wormhole generated. The description of wormhole process requires a number of equations shown below:

$$V_i = \frac{Q}{\frac{1}{4}*\pi*d_{Core}^2*\phi} \tag{1.7}$$

$$PV_{BT} = \frac{V_i}{V_{wh}} \tag{1.8}$$

$$V_{wh} = W_{eff} * V_i^{\frac{2}{3}} * B(V_i) \tag{1.9}$$

$$B(V_i) = (1 - \exp(-WB * V_i^2))^2 \tag{1.10}$$

Where vi is interstitial velocity, Q is flow rate, d is diameter of the core, ϕ is porosity, vwh is the velocity of the wormhole, and W_{eff} and W_B are wormhole efficiency and B factors. From experiments, $v_{i,opt}$ and $PV_{BT,opt}$ can be determined, and W_{eff} and W_B can be calculated directly,

$$W_{eff} = V_{i,opt}^{\frac{1}{3}} \tag{1.11}$$

$$WB = 4/V_{i,opt}^2 \tag{1.12}$$

Then the skin factor is calculated using this equation.

$$Skin = \frac{k_0}{k_{stim}-1} * \left(\ln\left(\frac{r_{wh}}{r_w}\right)\right) \ldots\ldots (1.13)$$

Where r_{wh} is the radius of the wormhole and can be calculated from v_{wh}, k0 and kstim are initial and stimulated permeability values. They conclude that these equations provide empirical value that can be deterministic of the wormhole growth process. However, the field scale application may have complications that are not accounted for in these empirical calculations which would hinder the accuracy in the predictions. From their work, it is recommended that the acid is to be pumped at the maximum rate below the fracturing pressure, as lower acid injection rate would result in face dissolution. This claim is questionable because at high rates, the wormhole structure is ramified with many branches, which is not the result for optimum efficiency.

There are relatively few results in literature for chemically retarded acid systems in carbonate rocks. Knox et al. in 1964 provides a general description of the use of chemically retarded acid in the field. Their work includes the laboratory scale experiments; many types of retarded acid systems including gel and emulsion as well as chemical means were tested. The result shows that chemically retarded acid provides the best retardation throughout rock types even at higher temperatures. Then they carried out multiple field experiments in various formations to confirm the versatility and applicability of chemically retarded acid systems.

Crowe et al. (1990) investigated the effect of multiple chemical retarders in their work. They tested eight different commercial chemicals mixed with HCl to see their retardation ability at 200 ° F and 1000 psi, and with kerosene-wet Indiana limestone and water-wet marble. The list of the chemicals they used is shown in Table 1.

Table 1. Retarder Types and Description (reprinted from Crowe et al. 1990)

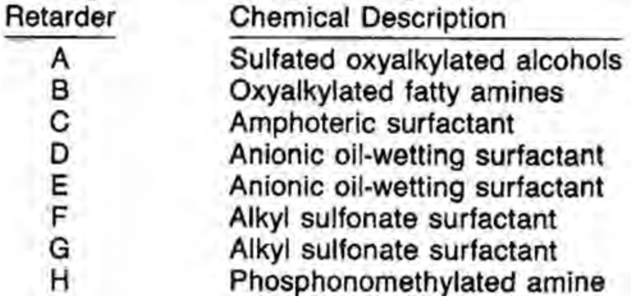

Retarder	Chemical Description
A	Sulfated oxyalkylated alcohols
B	Oxyalkylated fatty amines
C	Amphoteric surfactant
D	Anionic oil-wetting surfactant
E	Anionic oil-wetting surfactant
F	Alkyl sulfonate surfactant
G	Alkyl sulfonate surfactant
H	Phosphonomethylated amine

The experimental results were rather intuitive, as the surface conditions of the rocks had high impact on the retardation capabilities of the chemicals. For example, water-wetting surfactants used as acid retarders on oil-wet limestone actually increased the acid dissolution rate, because they stripped away the oil wet surface and enabled the acid to react with the limestone freely. Although they use chemical means to retard acid reaction, some of their chemicals acted as physical barriers similar to emulsion, rather than chemically inhibiting the protons.

Chang et al. (2008) investigated the effect of mixing organic acids with HCl to understand the effects in carbonate reservoirs. The study shows in depth dissolution chemistry by characterizing the equilibrium constants for the organic acids as they do not react completely as HCl does. The acids were modeled by measuring the electrolyte concentrations and the amount of CO_2 before and after the organic acids used in their work (acetic and formic) reached equilibrium. They mixed 15% HCl with 10 wt% acetic acid and 9 wt% formic acid, and carried out acid dissolution experiments to understand the dissolving powers of each mixture. As it can be seen in Figures 7 through 10, the mixed acids react more completely than organic acids alone, yet they slow down the highly corrosive HCl reaction, which enables deeper wormhole penetration than when HCl is used alone. When acetic acid and formic acid are used on their own, the amount of calcite dissolved by unit mass of acid is relatively low (~10kg for 10% acetic acid, and 12kg for 9% formic acid). However, when they are mixed with 15% HCl, the amount of dissolved calcite triples to about 35kg for both acids.

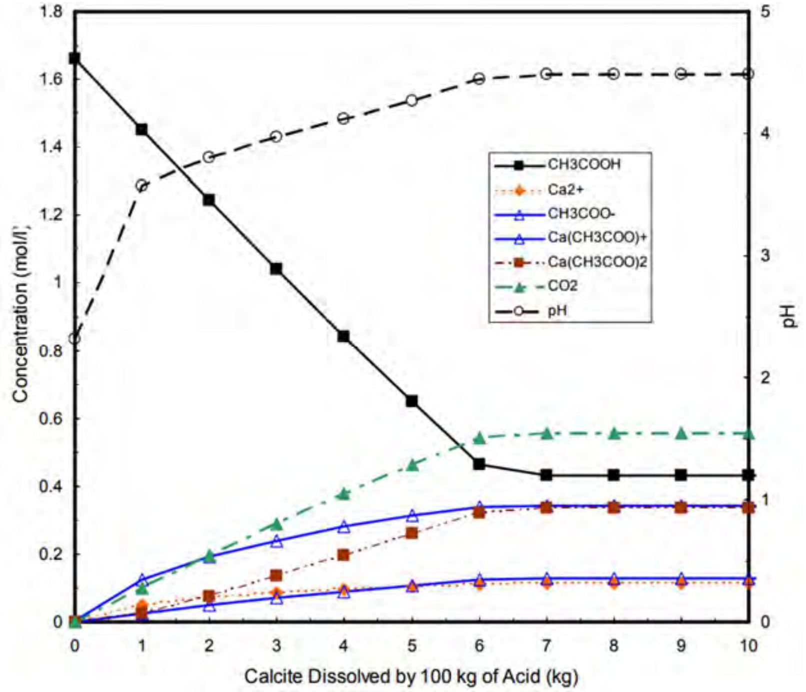

Figure 7. Equilibrium concentrations of 10 wt% acetic acid alone (reprinted from Chang et al. 2008).

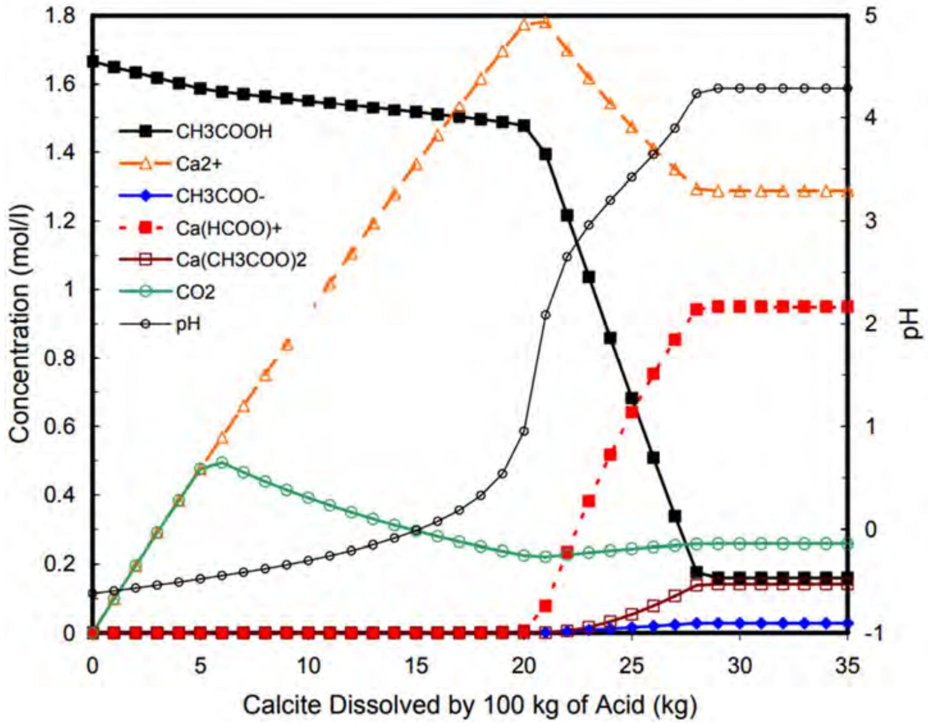

Figure 8. Equilibrium concentrations of 10 wt% acetic acid mixed with 15% HCl (reprinted from Chang et al. 2008).

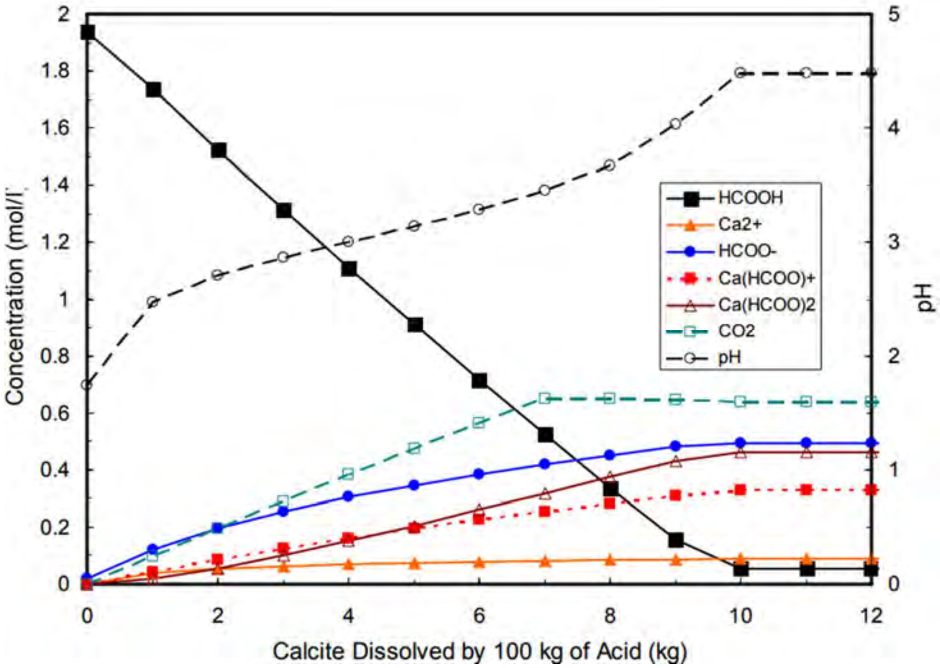

Figure 9. Equilibrium concentrations of 9 wt% formic acid alone (reprinted from Chang et al. 2008).

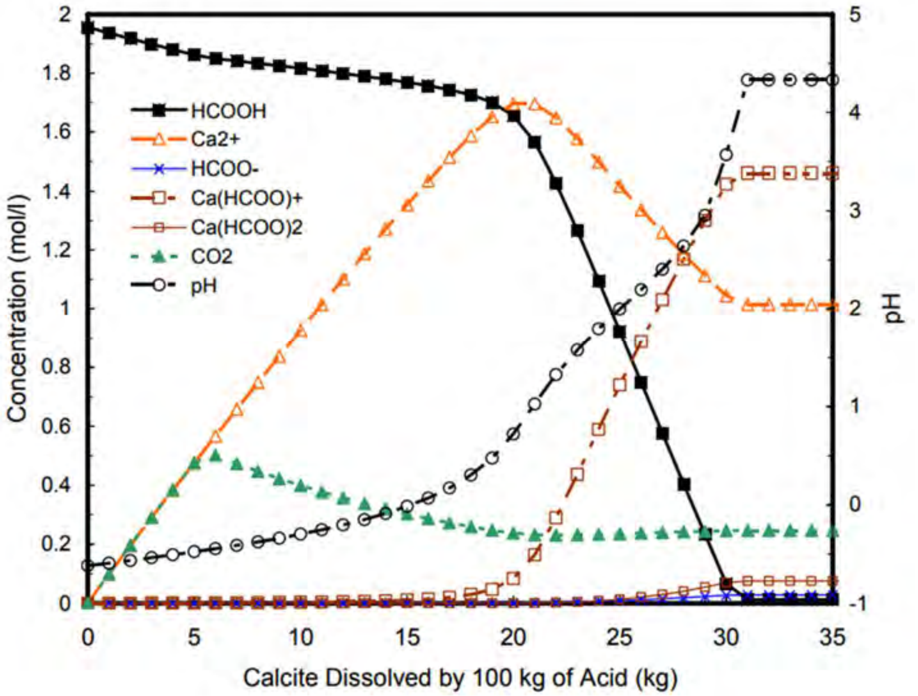

Figure 10. Equilibrium concentrations of 10 wt% acetic acid mixed with 15% HCl (reprinted from Chang et al. 2008).

These results show that the mixture of HCl and organic acids benefit each other by both increasing the organic acid dissociation and reducing the rapid reaction rate of HCl. This phenomena ultimately benefits the acidizing treatment by increasing the penetration length due to delayed dissociation.

Sokhanvarian et al. (2017) recently published their work on a new in-situ HCl based acid. This new acid entails 30 wt% HCl with undisclosed other chemical compounds. Coreflood experiments were conducted on carbonate cores (dolomite and limestone). Their results show the in-situ HCl was successful in increasing the permeability for carbonate rocks. Their limestone coreflood experiment results showed PV_{BT} of 1.35 for the new acid compared to PV_{BT} of 2.01 for 15% HCl as shown in Figure 11.

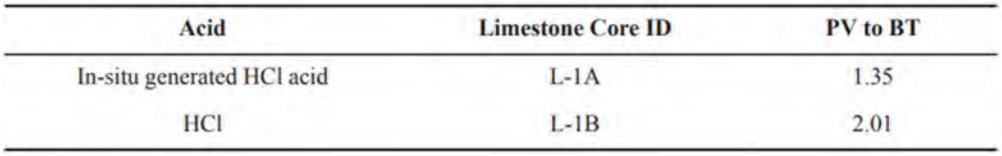

Acid	Limestone Core ID	PV to BT
In-situ generated HCl acid	L-1A	1.35
HCl	L-1B	2.01

Figure 11. Acidizing results for limestone cores at 2cm/min and 300˚F (reprinted from Sokhanvarian et al. 2017)

This shows that there is interest and active research being conducted for reducing the reactivity of HCl to enable better results of matrix acidizing. However, there is a lack of comprehensive study that links the wormholing phenomenon of chemically retarded acid to the field scale production improvement simulation.

1.3 Objective

In order to fully understand the impact of chemical retardation of acid reaction in matrix acidizing, a series of coreflood experiments were carried out. The properties of these acid systems must be analyzed and simulated in field scale to assess the reduction in skin factor as well as production improvement. The objective of this research can be defined as following:

1. Study wormhole efficiency of chemically retarded acids through core flood experiments to obtain their $PV_{BT,opt}$ and $v_{i,opt}$, compare with 15% HCl.
2. Calculate volumetric dissolving power constant to obtain each acid system's dissolution power relative to 15% HCl.
3. Simulate the acid in field scale using Buijse-Glasbergen wormhole modeling to analyze the impact of chemical retardation of acid reactivity in wormhole development and production rate.

2. EXPERIMENTAL APPARATUS

2.1 Experimental Apparatus Description

In order to run coreflood experiments, the laboratory equipments specifically designed for coreflood testing were used. This setup was initially designed and assembled by Grabski (2012) with syringe pump, hydraulic pump, water and acid accumulators, core holder, nitrogen tank and LabView software on PC. A diagram of this setup is shown below in Figure 12.

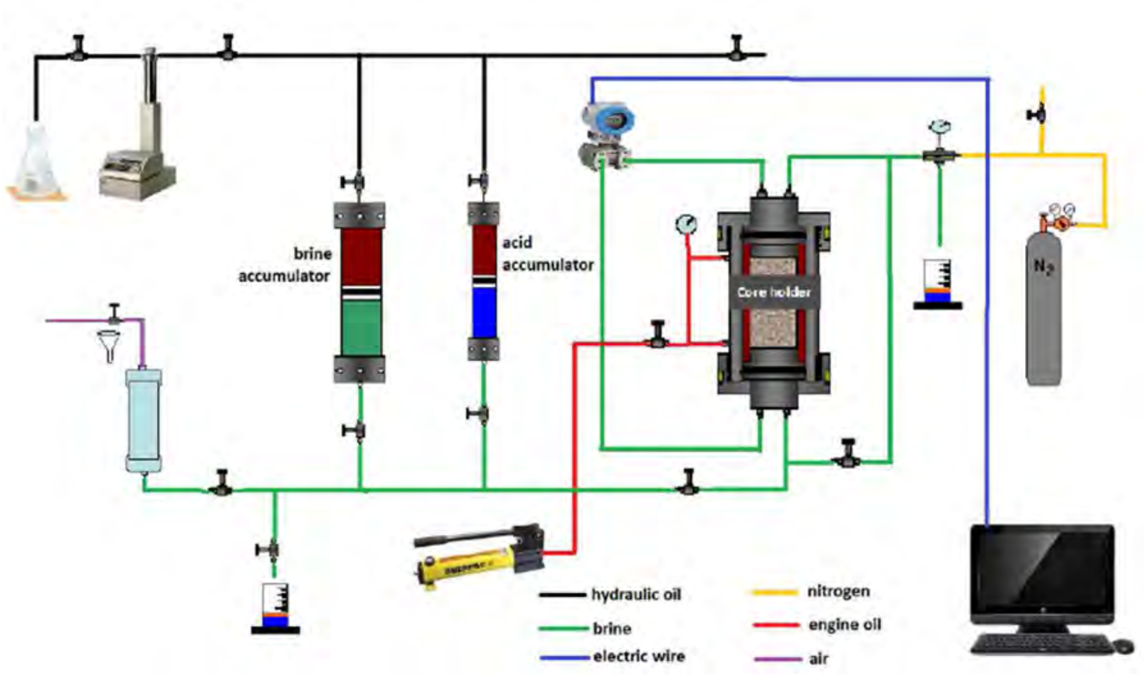

Figure 12. Coreflood experimental setup

2.2 Syringe Pump

The syringe pump (Figure 13) is from Teledyne, and is used to displace the fluid of choice into the system. It is capable of injection rates between 0.0001ml/min to 107ml/min with the maximum operating pressure of 7500 psi (Etten 2015). The experimental flow rates never exceeded 40ml/min so that there was enough pumping power to refill the pump for continuous flow. The pump used hydraulic oil that was pumped to either water or acid accumulator to displace the fluid. The pumping rate was controlled by the digital button input on the pump itself, and the pumping pressure was displayed for pressure monitoring.

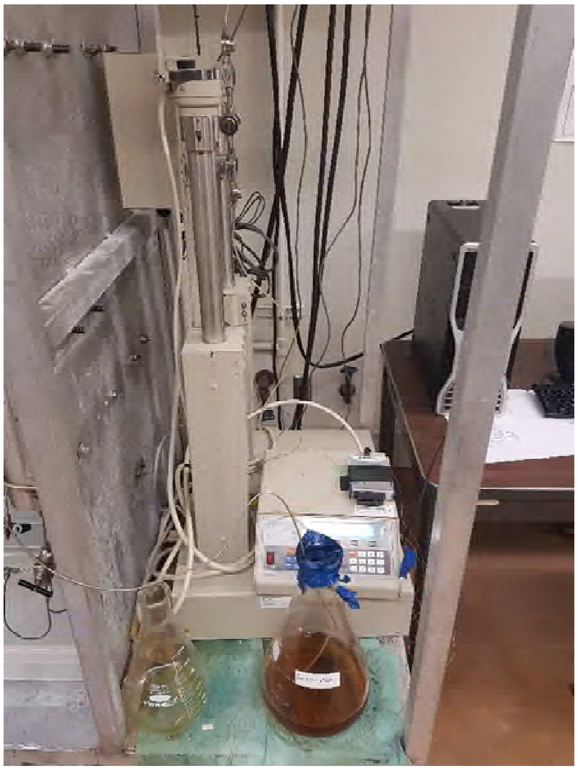

Figure 13. Syringe pump with oil reservoir flask

2.3 Accumulators

There are two accumulators that are connected to the inlet piping and syringe pump (Figure 14).

Figure 14. Acid (right) and water (left) accumulators with refill container (middle)

2.3.1 Water Accumulator

The water accumulator is made up of stainless steel 316 and has a capacity of 1 liter with pressure rating of 5000 psi. Inside, there is a piston that is controlled by the syringe pump at a set flow rate to ensure constant flow is achieved. To refill, the refill container is filled with water and the water is injected into the accumulator with pressured air.

2.3.2 Acid Accumulator

The acid accumulator is made up of Hastelloy C-276, which is corrosion resistant and fit for acidizing use. Similar to the water accumulator, there is a piston within the acid accumulator that is controlled by pressure and injection rate from the syringe pump. The acid accumulator is filled by pressured air through the refill container after it is filled with acid.

2.4 Hydraulic Pump

The hydraulic pump (Figure 15) was used to provide confining pressure for the core holder to generate a seal around the core during the experiment. It was connected to the core holder, and the oil was injected outside of the viton sleeve, and inside the metal core holder itself. The pump pressure was measured by the pressure gauge attached to the inlet, and it was desirable to maintain about 2500 psi, to exceed the 2000 psi back pressure and to stay below the 3000 psi the core holder casing is rated for.

Figure 15. Hydraulic pump

2.5 Core Holder

The core holder is the main piece of the experimental setup (Figure 16), in which the core is inserted and acid is injected. The hardware is made up of majorly three parts: outer casing, sleeve, and plugs. The outer casing is a cylinder that is pressure rated upto 3000 psi and temperature rated upto 300F.

Figure 16. Core holder

The viton sleeve is within the metal casing of the core holder, and holds the core in place with the help of hydraulic oil pump to apply the confining pressure. When the core holder is assembled with the core, the sleeve would form a seal around the core to ensure no acid bypasses the core. Sometimes, if the acid breaks out of the core on the side instead of the top of the core, the sleeve may break due to the high confining pressure usually kept around 2500 psi. The top and bottom plugs (Figure 17) are inserted and sealed before running the experiment. They both have piping connections: inlet and pressure transducer connections for the bottom plug, and outlet waste line and pressure transducer connection for the top plug.

Figure 17. Plugs for the core holder

When the core holder for experiments is completely assembled, the bottom plug fits into the core holder and is turned to seal. The top plug is inserted into the core holder and is screwed in with another metal cap to ensure a seal.

2.6 Back Pressure System

The back pressure of 2000 psi was achieved by controlling the nitrogen tank (Figure 19) connected to the back pressure regulator (Figure 18). When the tank is opened and set to 2000 psi, the nitrogen pressurizes the whole system to ensure CO_2 is kept within solution (Cheng et al. 2016). The back pressure regulator ensures that this pressure is maintained well throughout the experiment by showing the system pressure. It contains a diaphragm inside which would be pressed by the nitrogen gas provided at 2000 psi, and would allow the fluid from the system to pass only when the pressure exceeds this back pressure to lift up the diaphragm.

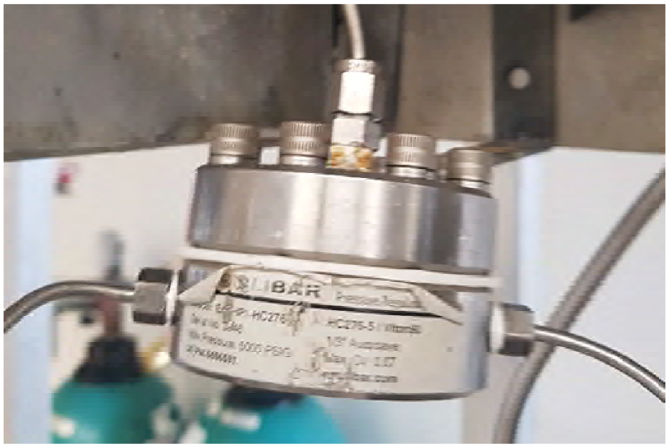

Figure 18. Back Pressure Regulator

Figure 19. Nitrogen tank

2.7 Heating System

The experiments were run at an elevated temperature of 180˚F or 82˚C. Two temperature measuring devices were used in the experimental setup. One was attached to the piping that attaches to the inlet piping of the core holder (bottom circle in Figure 20) to ensure the fluid entering the core holder was at desired temperature. The other one was attached to the core holder to monitor the core holder temperature shown in top circle in Figure 20. In order to achieve the desired temperature, two heating tapes from Omega Engineering were used to heat up the system as well as two thermocouple probes to monitor the temperature. As seen in Figure 20,

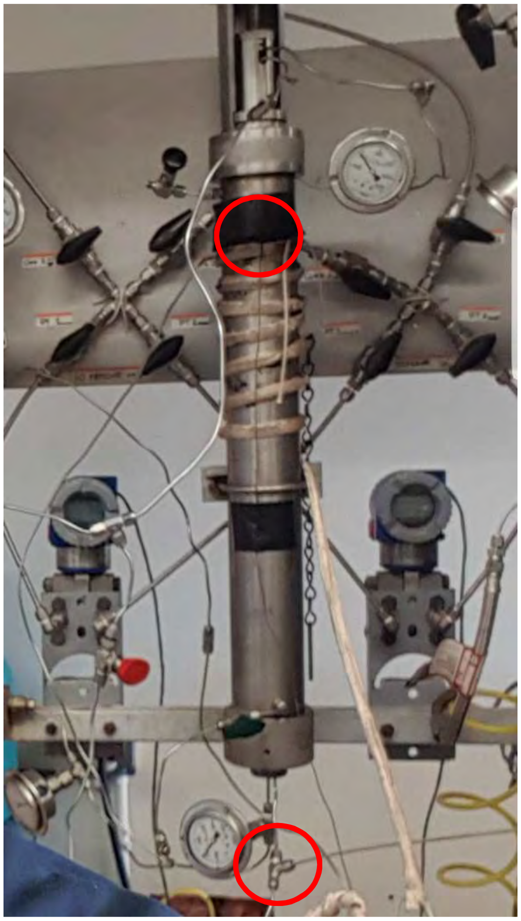

Figure 20. Core holder with heating tape

one heating tape was wrapped around the core holder to heat up the core holder directly from outside. Another heating tape was wrapped around the piping (Figure 21) that connects to the bottom of the core holder to heat up the fluid entering the system. Left circle is the part that connects to the inlet of the core holder and right circle is the part that connects to the accumulator outlets. The heating tapes were controlled by LabView software from the PC.

Figure 21. Heating Tape on Fluid Piping

These heating tapes and sensors were connected to the PC via a collection module as seen in Figure 22 and their operations were controlled automatically by LabView software.

Figure 22. Data acquisition module

2.8 LabView

LabView software is used to monitor and control the temperature and pressure data from the experimental setup. The temperature data came from the two temperature probes located on the inlet and core holder. Pressure data comes from the pressure gauges installed at the outlet of the core holder. In each experiment, a LabView file is saved for all of the pressure and temperature data. Also, the heating tape operations are controlled within the LabView interface automatically.

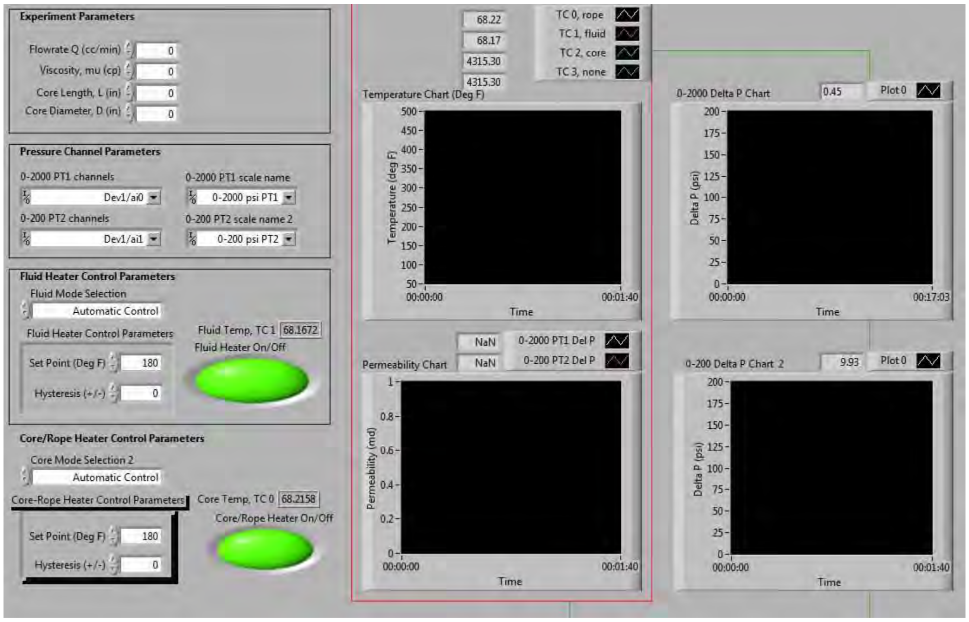

Experiment Parameters

Flowrate Q (cc/min) 0
Viscosity, mu (cp) 0
Core Length, L (in) 0
Core Diameter, D (in) 0

Pressure Channel Parameters

0-2000 PT1 channels Dev1/ai0
0-2000 PT1 scale name 0-2000 psi PT1
0-200 PT2 channels Dev1/ai1
0-200 PT2 scale name 2 0-200 psi PT2

Fluid Heater Control Parameters

Fluid Mode Selection Automatic Control
Fluid Heater Control Parameters
Set Point (Deg F) 180
Hysteresis (+/-) 0
Fluid Temp, TC 1 68.1672

Core/Rope Heater Control Parameters

Core Mode Selection 2 Automatic Control
Core-Rope Heater Control Parameters
Set Point (Deg F) 180
Hysteresis (+/-) 0
Core Temp, TC 0 68.2158

TC 0, rope 68.22
TC 1, fluid 68.17
TC 2, core 4315.30
TC 3, none 4315.30
0-2000 PT1 Del P NaN
0-200 PT2 Del P NaN
0-2000 Delta P Chart Plot 0 0.45
0-200 Delta P Chart 2 Plot 0 9.93

Figure 23. LabView Interface

As shown in Figure 23, when the set points are inputted, the LabView software controls the heating operation. Light green indicates the system turning on the heating tape connected to the control to increase the temperature to meet the set point.

3. EXPERIMENTAL PROCEDURE

This section reviews the experimental preparation, matrix acidizing experiment, and post-experiment data analysis procedures. A total of thirty matrix acidizing experiments were conducted for three different novel acid systems and 15% HCl. All were conducted with Indiana limestone cores at elevated temperature and pressure (180˚F and 2000psi).

3.1 Experimental Preparation

Experimental preparation step is crucial before conducting any experiment. Especially for the matrix acidizing, proper saturation of the cores and preparation of the correct concentration of acids must take place every time.

3.1.1 Core Preparation

Once the cores are cut in correct dimensions, the following procedure is used for pre-experiment core preparation.

1. Label cores.
2. Dry cores overnight in the oven, for at least 12 hours.
3. Weigh the dry cores, record weight.
4. Saturate the cores with water for 6 hours.
5. Weigh and record the saturated cores.
6. Calculate the porosity, and store the cores in water until the experiment

To dry the cores, a tabletop oven was used. The cores were saturated under water with a glass bowl connected to a pump. The cores were submerged in water and the vacuum pump ensured all of the air within pores was extracted. The porosity of the cores was calculated by measuring dry and wet weights.

$$\phi = \frac{V_{pore}}{V_{bulk}} \times 100\ (\%) \qquad (3.1)$$

$$V_{pore} = \frac{M_{sat} - M_{dry}}{\rho_{brine}} \qquad (3.2)$$

$$V_{bulk} = \frac{1}{4}\pi d^2 * L \qquad (3.3)$$

3.1.2 Acid Preparation

For the experiments, each acid was prepared with 3 vol % corrosion inhibitor from Schlumberger. Hydrochloric acid was diluted from 36wt% to 15wt% by adding deionized water. The other acids, HCR-6000, 7000, and 8000 were received from the manufacturer ready-to-use. They were also mixed with 3 vol % corrosion inhibitor before the experiment.

3.2 Overall Experimental Procedure

The overall experimental schematic is shown in Figure 24, and the valve numbers in the following sections can be referred to this diagram. The experimental procedure can be largely divided into three sections: system preparation, running experiment, and disassembly.

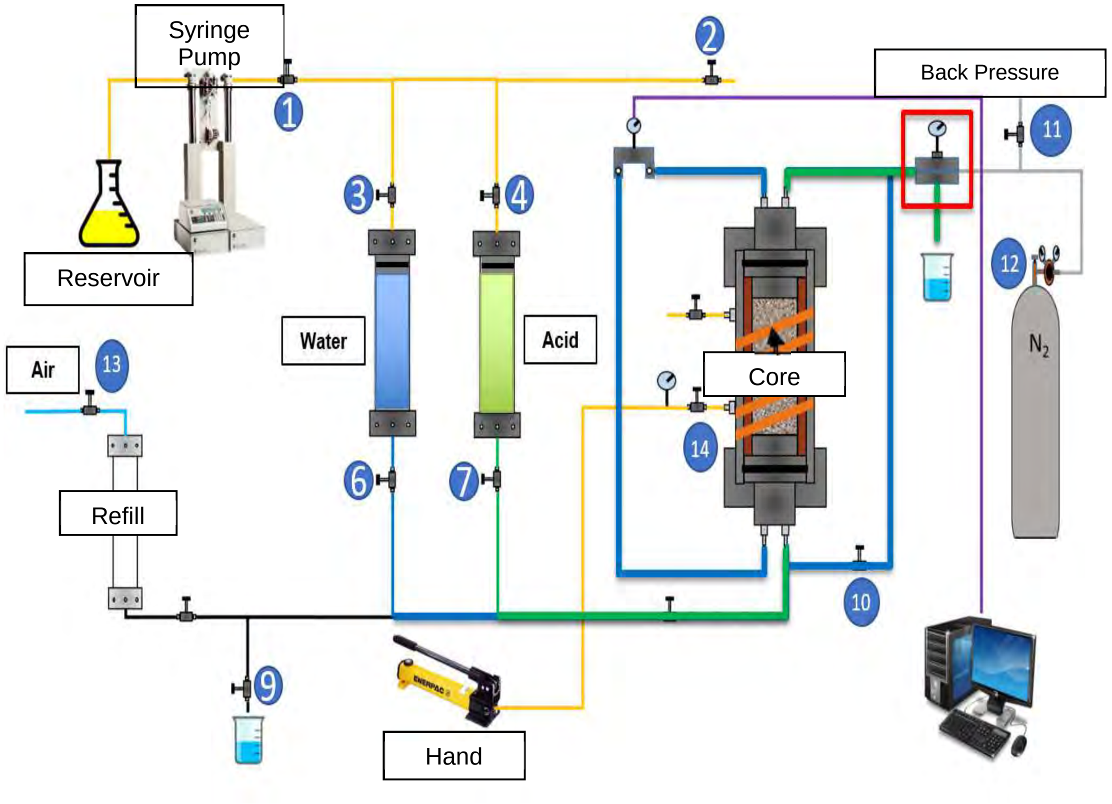

Figure 24. Coreflood Experimental Setup Schematic

3.2.1 System Preparation

The entire system must be depressurized before running any new experiment. The pressure gauges should read 0 psi or lower on all gauges. Make sure the syringe pump pressure reading is also below 0 psi. After ensuring the system has no pressure build up within, the accumulators may be filled. The accumulator filling step should follow this work flow.

- Acid Accumulator Preparation Steps:
    1. Check to see the refill tank is empty
    2. Remove stopper and place funnel on refill tank
    3. Fill the refill tank with prepared acid

4. Remove funnel and put stopper
5. Open oil recycle valve (#2) and check (#6, #8) are closed
6. Turn on Air Supply using Air Supply Valve (#13)
7. Adjust Acid Accumulator Valve (#7) to allow refill
8. Note: If Acid Accumulator is being filled, oil should flow into reservoir flask
9. Close Acid Accumulator Valve (#7) when liquid level in refill tank is low [approximately 1 in from the bottom]. To avoid air from entering Acid Accumulator do not empty refill tank.
10. Once refill Acid Accumulator Valve (#7) is closed, do not open it until all acid is drained from acid accumulator.
11. Turn off Air Supply Valve (#13)
12. Close Oil Recycle Valve (#2)
13. Adjust Acid Accumulator Valve (#7) to allow inject at 2 ml/min, check Valve (#10) is closed, acid should come out of the only exit available.
14. Once steady flow comes, close Valve (#7)

After this step, the acid accumulator is filled and ready for the experiment. Next step is to fill the water accumulator. The reason to fill the acid accumulator first is to ensure the shared piping is clear of acids before actually injecting acid for the experiment.

- Water Accumulator Preparation:
  1. Remove stopper and place funnel on refill tank
  2. Fill refill tank with water to desired level
  3. Remove funnel and replace stopper
  4. Open Oil Recycle Valve (#2)

5. Check all values (#7,8,9) are completely closed
6. Turn on Air Supply using Air Supply Valve (#13)
7. Adjust Water Accumulator Valve (#6) to allow refill
8. Note: If Water Accumulator is being filled, oil should flow into reservoir flask
9. Close Water Accumulator Valve (#6) when water level in refill tank is low [approximately 1 in from the bottom]. To avoid air from entering Water Accumulator do not empty refill tank.
10. Turn off air supply
11. Repeat until Water Accumulator is filled with desired water volume
12. Close Oil Recycle Valve (#2)
13. Check Valve (#10) is closed and inject water to only available exist until pH paper no longer detect acid.
14. Open Valve (#10) and use finger to close the exit in previous step to allow flow through Valve (#10). Flow until acid no longer detected with pH paper.

Now, the accumulators are both filled and are ready for the experiment. The next step is to assemble the core holder and connect the piping.

- Core Holder Assembly:
    1. Clean Core Holder and all components by rinsing with water
    2. Insert core into the core holder
    3. Insert bottom plug and twist right to secure
    4. Insert top plug until snug fit
    5. Place and screw in top cap
    6. 1.5” core holder: mount core holder onto rig

7. Connect fluid and core heater plugs
8. Tape thermocouple on to core heater to measure core holder temperature.
9. Make sure a second thermocouple is properly connected to a 3-way at the inlet

- Connecting Pipings to the Core Holder:

1. Select Pressure Transducer [0 to 2000 psi or 0 to 200 psi] by opening/closing valves connected to the pressure transducer
2. Adjust Water Accumulator Valve (#6) to allow injection
3. Adjust flow rate to 2ml/min and run pump
4. Make the following connections with water flowing and in this particular order (Allow flow to come out of each connection before connecting)
5. Core Inlet Tubing
6. Core Inlet Pressure Gauge
7. Confining Pressure Tubing
8. Open Confining Pressure Valve (#15) and add 500 psi of confining pressure using the hand pump
9. Make the following connections with water flowing and in this particular order (Allow flow to come out of each connection before connecting):
10. Core Outlet Tubing
11. Core Outlet Pressure Gauge
12. Add Back Pressure
13. Open Nitrogen Tank Valve (#12) until air flows through Bypass Valve (#11)
14. Close Bypass Valve (#11)

15. Continue to open Nitrogen Tank Valve (#12) to add 500 psi of backpressure (for permeability test) and 1200 psi of backpressure (for matrix acidizing) - This will cause pump injection pressure to rise, make sure to maintain confining pressure 500 psi above pump injection pressure
16. Check system for leaks and start LabView

Now, the experimental preparation steps are complete. All equipment are set up for permeability test and acid injection.

3.2.2. Conducting Experiment

The experiment begins with measuring the permeability of the core. A permeability test is conducted before every acid injection to gather a permeability value for the core.

- Permeability Test Steps:

1. Adjust pump to desired flow rate
2. Record Baseline pressure (the pressure on the transducer before closing the bypass) while water is flowing through bypass line
3. Close Bypass Valve (#10)
4. This will cause pump injection pressure to rise, make sure to maintain confining pressure 500 psi above pump injection pressure
5. Once constant, record pressure drop across the core and use this to calculate permeability

From this pressure drop, the permeability of the core can be calculated using a modified form of Darcy's Law of permeability:

$$k = \frac{122.63*q*L*\mu}{\Delta P*d^2} \quad (3.4)$$

in which the q is flow rate in cm^3/min, L is the length of the core in inches, μ is fluid viscosity in cp, P is pressure in psi, d is the core diameter in inches.

After the permeability is assessed, the temperature must be increased and needs to stabilize. The acid can be injected when the desired temperature is reached.

- Acid Injection:
    1. Increase temperature controls in LabView to 180˚F (82˚C)
    2. Wait for thermocouple to detect desired temperature
    3. Release oil through needle valve in core holder as confining pressure increase due to oil expansion as temperature increases.
    4. Once both core holder and fluid heater both reaches desired temperature, continue with injection steps
    5. Simultaneously adjust Acid Accumulator Valve (#7) to inject, close Water Accumulator Valve (#6) and start timer
    6. Once pressure drop across the core becomes negligible, simultaneously stop timer and close Acid Valve (#7) and open Water Accumulator Valve (#6)
    7. Allow water to flow through core for a few minutes, test outlet with pH test, make sure no acid left.

At this stage, the main part of the experiment is finished. The experimental setup can now be disassembled, and core can be analyzed.

3.2.3 Disassembly and Core Analysis

- The disassembly procedure is as following:
  1. Depressurize entire system
  2. Stop syringe pump
  3. Release Hand Pump Valve (#14) and Backpressure Valve (#12)
  4. Open Oil Recycle Valve (#2)
  5. Check to see that all pressure gauges read 0 psi or lower
  6. Disconnect in same order connections were made
  7. Use Proper PPE to remove core holder due to high temperature
  8. Remove Core Holder
  9. Drain remaining water from Water Accumulator into a bucket
  10. Empty bucket into disposal container

And now, the coreflood experiment is finished and the cores must be analyzed further. There are two major assessments that the cores need to go through after acidizing: dry weight measurement and CT scanning for wormhole images.

- Dry Weight Measurement Procedure:
  1. Put cores into the tabletop oven
  2. Dry it overnight
  3. Measure dry weights of the cores

The CT scanning and image processing procedure follows the workflow composed by Frick in 2016.

- CT Scan & Image Processing:
  1. Contact CT scanner operator and scan the cores

2. Wait for the scanned images to be uploaded on server
3. Open ImageJ → Plugins → Tudor DICOM → DICOM Manager
4. Click folder icon (first on the left) in DICOM Manager
5. In new window, click DICOM QUERY → click search icon (top right corner)
6. Look for “Patient Name” along with “Patient ID” to identify correct core
7. Click on desired core → click on “Study ID” → click on “Retrieve to Local”
8. Find file saved in Home (H:) → DICOMSTORE → “Patient Name”
9. Download files to desired storage device (USB etc.)
10. Transfer files from storage device to desired location on Mac computer
11. Open Horos → Click “Import” → Find desire file and click “open”
12. Option box will ask “Copy files or copy links” → Click “Copy Links” to save memory space
13. For 3D volume rendering, open the 3rd image set and start from the 1st image of the set
14. Click “Oval Tool” → Manipulate oval to fit core image → Click “Propagate Selected ROI”
15. Under “Propagate current selected ROI(s) to:” select up to image number → Enter 100 or other necessary value to fit oval on core
16. Under “Copy Method” select “Create Aliases” → Click Ok
17. For the last set of propagated ROIs, the ROI will need to be propagated to the total number of images minus 1 image number
18. Click “ROI” → Click “Save All ROIs of this Series”
19. Save ROI in desired location as “Core ID ROI”

20. Click “ROI” → Click “Set pixels values too” → Under “Apply to:” select “ROIs with same name as the selected ROI
21. Under “Set pixels that are:” select “Outside ROI”
22. Select “To this new value:” and enter “3024” → Click Ok
23. Click “3D Viewer” → Click “3D Volume Rendering”
24. Change level of detail to “Fine” on the toolbar
25. Select “16 bit” and histogram will appear at bottom of the screen
26. Move points within histogram to reveal dissolution structure → Double click on all points and change all points to 100% Whiteness
27. Once the desired level of clarity is achieved, Click “16 bit”, and the histogram will disappear
28. Click “Magnifying Glass” icon to change zoom level to 0.125%
29. Click “File” → Click “Export” → Click “Export to Movie”
30. Set “Number of frames:” to 360 → Under “Rotation:” select “360 degrees” and “Horizontal” → Under “Quality:” select “Best rendering” → Under “Size:” select “Current” → Click Ok
31. Adjust “Frame rate:” to desired level (Default value = 20)
32. Under “Format:” select “H264 Movie”
33. Name file as “Core ID HiRes” → Click Save
34. Click “Measurement Tool” and measure length of wormholes (if not brokenthrough) → Make sure line is vertically straight for accurate measurement
35. Click “File” → Click “Export” → Click “Export to JPEG”

The CT scanned images of the cores are available at this point and the wormhole structure can be analyzed.

4. RESULTS AND DISCUSSION

4.1 Experimental Data Analysis

The experimental result analysis followed a general workflow. During the experiment, a comprehensive excel sheet (shown in Figure 25) containing all of the parameters required for analysis is filled. The parameters recorded included: back pressure, dry and wet weight of the cores, permeability, porosity, acid injection rate, interstitial velocity, and pore volume to breakthrough.

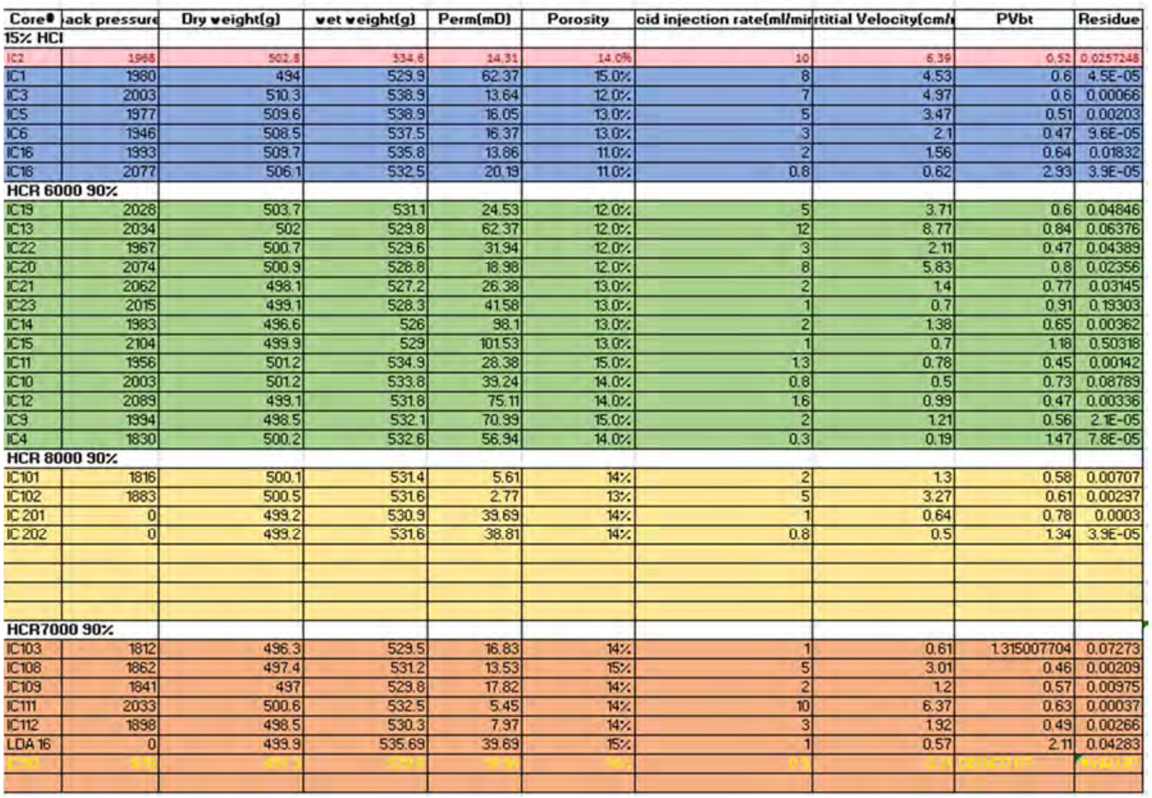

Core#	ack pressure	Dry weight(g)	wet weight(g)	Perm(mD)	Porosity	cid injection rate(ml/mir	rtitial Velocity(cm/	PVbt	Residue
15% HCl									
IC2	1966	502.8	534.6	14.31	14.0%	10	6.39	0.52	0.0257248
IC1	1980	494	529.9	62.37	15.0%	8	4.53	0.6	4.5E-05
IC3	2003	510.3	538.9	13.64	12.0%	7	4.97	0.6	0.00066
IC5	1977	509.6	538.9	16.05	13.0%	5	3.47	0.51	0.00203
IC6	1946	508.5	537.5	16.37	13.0%	3	2.1	0.47	9.6E-05
IC16	1993	509.7	535.8	13.86	11.0%	2	1.56	0.64	0.01832
IC16	2077	506.1	532.5	20.19	11.0%	0.8	0.62	2.93	3.9E-05
HCR 6000 90%									
IC19	2028	503.7	531.1	24.53	12.0%	5	3.71	0.6	0.04846
IC13	2034	502	529.8	62.37	12.0%	12	8.77	0.84	0.06376
IC22	1967	500.7	529.6	31.94	12.0%	3	2.11	0.47	0.04389
IC20	2074	500.9	528.8	18.98	12.0%	8	5.83	0.8	0.02356
IC21	2062	498.1	527.2	26.38	13.0%	2	1.4	0.77	0.03145
IC23	2015	499.1	528.3	41.58	13.0%	1	0.7	0.91	0.19303
IC14	1983	496.6	526	98.1	13.0%	2	1.38	0.65	0.00362
IC15	2104	499.9	529	101.53	13.0%	1	0.7	1.18	0.50318
IC11	1956	501.2	534.9	28.38	15.0%	1.3	0.78	0.45	0.00142
IC10	2003	501.2	533.8	39.24	14.0%	0.8	0.5	0.73	0.08789
IC12	2089	499.1	531.8	75.11	14.0%	1.6	0.99	0.47	0.00336
IC9	1994	498.5	532.1	70.99	15.0%	2	1.21	0.56	2.1E-05
IC4	1830	500.2	532.6	56.94	14.0%	0.3	0.19	1.47	7.8E-05
HCR 8000 90%									
IC101	1816	500.1	531.4	5.61	14%	2	1.3	0.58	0.00707
IC102	1883	500.5	531.6	2.77	13%	5	3.27	0.61	0.00297
IC 201	0	499.2	530.9	39.69	14%	1	0.64	0.78	0.0003
IC 202	0	499.2	531.6	38.81	14%	0.8	0.5	1.34	3.9E-05
HCR7000 90%									
IC103	1812	496.3	529.5	16.83	14%	1	0.61	1.315007704	0.07273
IC108	1862	497.4	531.2	13.53	15%	5	3.01	0.46	0.00209
IC109	1841	497	529.8	17.82	14%	2	1.2	0.57	0.00975
IC111	2033	500.6	532.5	5.45	14%	10	6.37	0.63	0.00037
IC112	1898	498.5	530.3	7.97	14%	3	1.92	0.49	0.00266
LDA 16	0	499.9	535.69	39.69	15%	1	0.57	2.11	0.04283
[illegible]	[illegible]	497.3	[illegible]	[illegible]	14%	0.5	0.31	[illegible]	#VALUE!

Figure 25. Comprehensive excel sheet

Also, a general worksheet that had basic calculation functions for interstitial velocity and pore volume to breakthrough was used for all experiments (Figure 26).

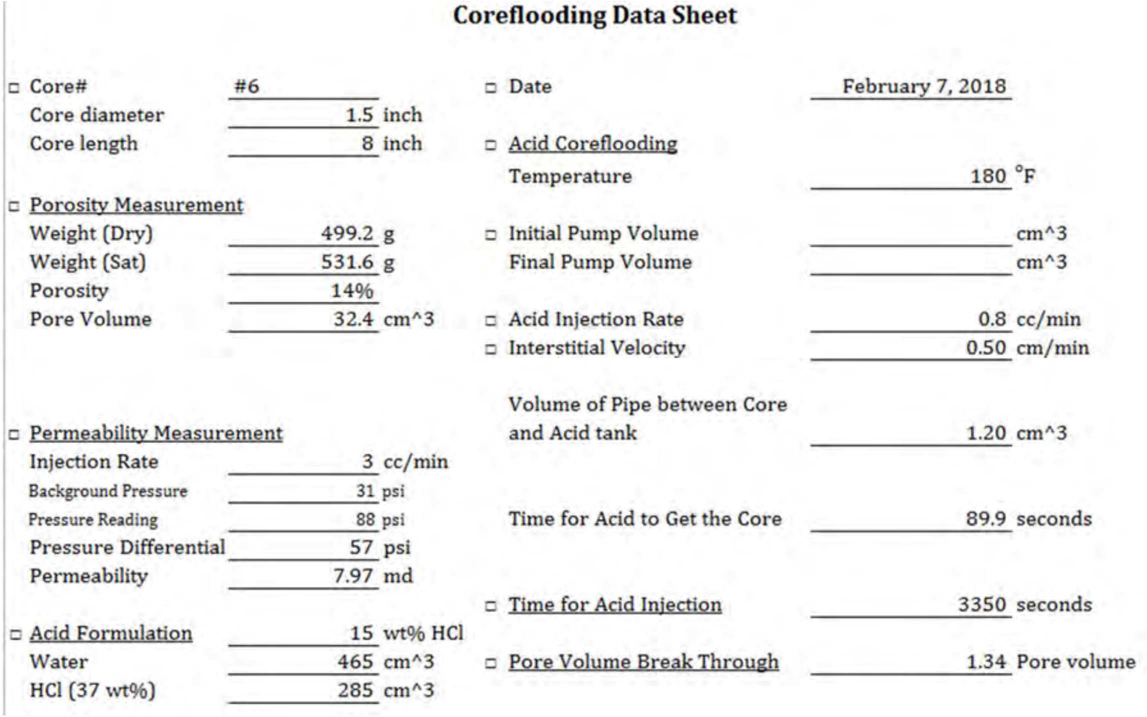

Coreflooding Data Sheet

☐ Core# #6
Core diameter 1.5 inch
Core length 8 inch

☐ Porosity Measurement
Weight (Dry) 499.2 g
Weight (Sat) 531.6 g
Porosity 14%
Pore Volume 32.4 cm^3

☐ Permeability Measurement
Injection Rate 3 cc/min
Background Pressure 31 psi
Pressure Reading 88 psi
Pressure Differential 57 psi
Permeability 7.97 md

☐ Acid Formulation 15 wt% HCl
Water 465 cm^3
HCl (37 wt%) 285 cm^3

☐ Date February 7, 2018

☐ Acid Coreflooding
Temperature 180 °F

☐ Initial Pump Volume ____ cm^3
Final Pump Volume ____ cm^3

☐ Acid Injection Rate 0.8 cc/min
☐ Interstitial Velocity 0.50 cm/min

Volume of Pipe between Core and Acid tank 1.20 cm^3

Time for Acid to Get the Core 89.9 seconds

☐ Time for Acid Injection 3350 seconds

☐ Pore Volume Break Through 1.34 Pore volume

Figure 26. Calculation page for various parameters

The interstitial velocity, which is the actual velocity of the fluid going through the pore space of the core, was calculated using these equations:

$$v_i = \frac{q}{A*\phi} \ldots\ldots\ldots\ldots\ldots\ldots\ldots\ldots\ldots\ldots\ldots\ldots\ldots\ldots\ldots\ldots\ldots\ldots (4.1)$$

where q is the flow rate, A is the surface area, and ϕ is the porosity. The pore volume to breakthrough is the amount of acid for wormhole to break through the core from one end to another. It is calculated using this set of equations:

$$PV_{BT} = \frac{V_{acid}}{V_{pore}} \tag{4.2}$$

For each core, interstitial velocity and pore volume to break through values were plotted. Then, the data points were curve fitted with Buijse-Glasbergen model, and these equations below were used to generate the curve fit for the data set of each acid.

$$PV_{BT} = \frac{v_i^{\frac{1}{3}}}{W_{eff} * B(v_i)} \tag{4.3}$$

$$W_{eff} = \frac{v_{i,opt}^{\frac{1}{3}}}{PV_{BT,opt}} \tag{4.4}$$

$$B(v_i) = \left(1 - \mathrm{e}^{\left(-\mathrm{W_B} * v_i^2\right)^2}\right) \tag{4.5}$$

$$W_B = \frac{4}{v_{i,opt}^2} \tag{4.6}$$

where W_{eff}, the wormhole efficiency factor, and W_B, the wormhole B-factor are used to calculate the optimal conditions. The optimal pore volume to breakthrough and interstitial velocity values were determined by minimizing the J value from equation (5.7). This was done by excel solver function as seen in Figure 27 below. The calculated data is then fitted onto the chart as a curve reflecting the optimal conditions from the experimental data.

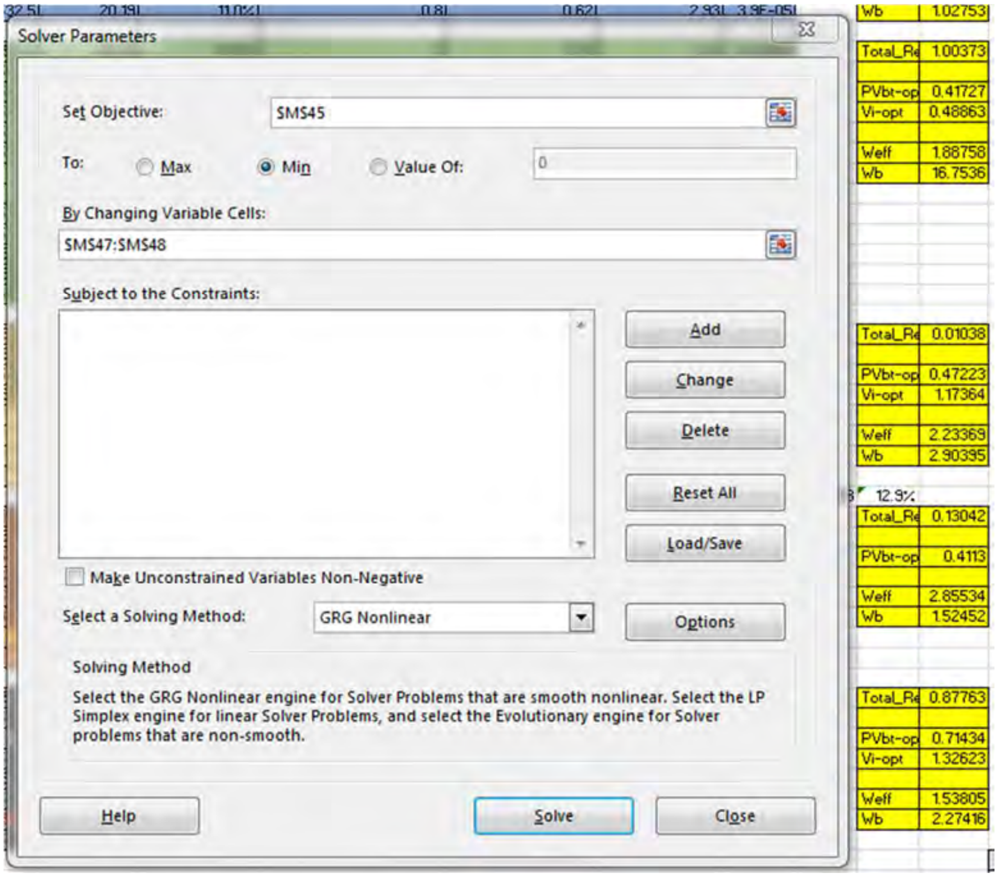
Solver Parameters

Set Objective: $M$45

To: ○ Max ● Min ○ Value Of: 0

By Changing Variable Cells: $M$47:$M$48

Subject to the Constraints:

☐ Make Unconstrained Variables Non-Negative

Select a Solving Method: GRG Nonlinear

Solving Method

Select the GRG Nonlinear engine for Solver Problems that are smooth nonlinear. Select the LP Simplex engine for linear Solver Problems, and select the Evolutionary engine for Solver problems that are non-smooth.

Wb	1.02753
Total_Re	1.00373
PVbt-op	0.41727
Vi-opt	0.48863
Weff	1.88758
Wb	16.7536
Total_Re	0.01038
PVbt-op	0.47223
Vi-opt	1.17364
Weff	2.23369
Wb	2.90395
	12.9%
Total_Re	0.13042
PVbt-op	0.4113
Weff	2.85534
Wb	1.52452
Total_Re	0.87763
PVbt-op	0.71434
Vi-opt	1.32623
Weff	1.53805
Wb	2.27416

Figure 27. Excel solver calculation for optimal conditions

4.1.1 HCl Core Flood Experiment Results

The properties of the cores used in the 15% HCl experiments are shown below in Table 2.

Table 2. 15% HCl Core Properties

Core#	Dry Weight(g)	Wet Weight(g)	Perm(mD)	Porosity
IC2	502.8	534.6	14.31	14.0%
IC1	494.0	529.9	62.37	15.0%
IC3	510.3	538.9	13.64	12.0%
IC5	509.6	538.9	16.05	13.0%
IC6	508.5	537.5	16.37	13.0%
IC16	509.7	535.8	13.86	11.0%
IC18	506.1	532.5	20.19	11.0%

Experimental results for HCl are shown below in Table 3. Total of seven cores were used to gather the data to generate the wormhole efficiency curve. The interstitial velocity and pore volume to breakthrough data can be seen in Table 3.

Table 3. 15% HCl Experimental Results

Core#	Acid injection rate (ml/min)	Interstitial Velocity (cm/min)	Pore Volume to Breakthrough	Perm(mD)
IC2	10	6.39	0.52	14.31
IC1	8	4.53	0.60	62.37
IC3	7	4.97	0.60	13.64
IC5	5	3.47	0.51	16.05
IC6	3	2.10	0.47	16.37
IC16	2	1.56	0.64	13.86
IC18	0.8	0.62	2.93	20.19

The optimal conditions for 15% HCl were then calculated from the Buijse-Glasbergen model curve fitting, and it is shown below in Table 4 with the generated curve in Figure 28.

Table 4. Optimal Condition for 15% HCl

	HCl
Optimal Pore Volume to Breakthrough	0.46
Optimal Interstitial Velocity (cm/min)	1.97

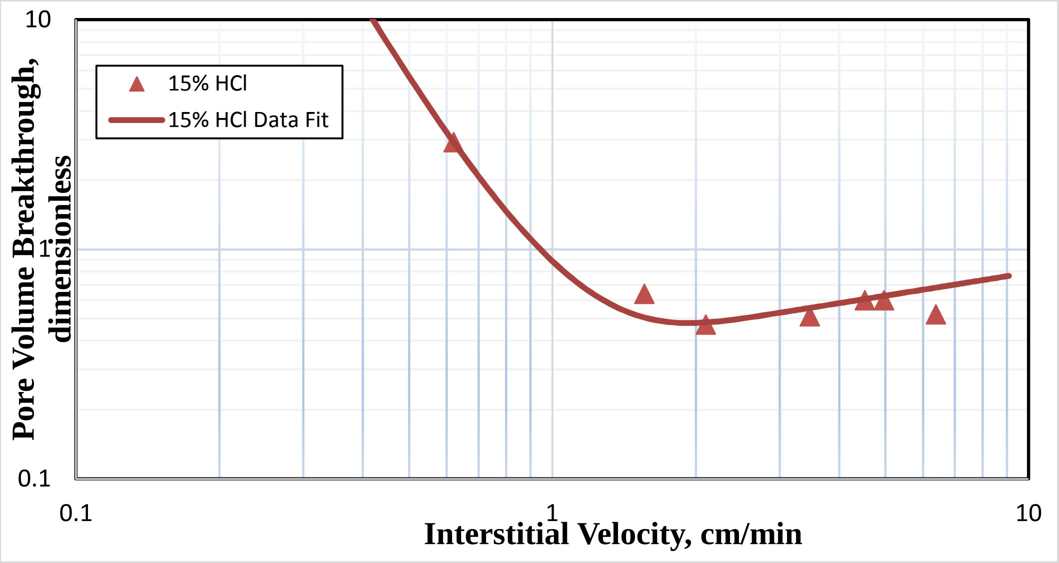

Figure 28. 15% HCl Acid Flux Curve

The images of the cores after acidizing experiment can be found in Appendix A.

4.1.2 HCR-6000 Core Flood Experiment Results

The properties of the cores used in the HCR-6000 experiments are shown in Table 5. The average porosity was 13%, and average permeability was 52.5 mD.

Table 5. HCR-6000 Core Properties

Core#	Dry Weight(g)	wet weight(g)	Perm(mD)	Porosity
IC19	503.7	531.1	24.53	12.0%
IC13	502.0	529.8	62.37	12.0%
IC22	500.7	529.6	31.94	12.0%
IC20	500.9	528.8	18.98	12.0%
IC21	498.1	527.2	26.38	13.0%
IC17	496.9	525.8	52.60	12.0%
IC14	496.6	526.0	98.10	13.0%
IC15	499.9	529.0	101.53	13.0%
IC11	501.2	534.9	28.38	15.0%
IC10	501.2	533.8	39.24	14.0%
IC12	499.1	531.8	75.11	14.0%
IC9	498.5	532.1	70.99	15.0%
IC4	500.2	532.6	56.94	14.0%

The experimental results showing the pore volume to breakthrough values corresponding to the interstitial velocity are shown in Table 6 and 7. The curve generated from Buijse-Glasbergen model as well as the individual experimental data points can also be seen in Figure 29.

Table 6. HCR-6000 Experimental Results

Core#	Acid injection rate (ml/min)	Interstitial Velocity (cm/min)	Pore Volume to Breakthrough	Perm(mD)
IC19	5	3.71	0.60	24.53
IC13	12	8.77	0.84	62.37
IC22	3	2.11	0.47	31.94
IC20	8	5.83	0.80	18.98
IC21	2	1.40	0.77	26.38
IC17	1	0.70	0.91	52.60
IC14	2	1.38	0.65	98.10
IC15	1	0.70	1.18	101.53
IC11	1.3	0.78	0.45	28.38
IC10	0.8	0.50	0.73	39.24
IC12	1.6	0.99	0.47	75.11
IC9	2	1.21	0.56	70.99
IC4	0.3	0.19	1.47	56.94

Table 7. Optimal Condition Comparison between HCl and HCR-6000

	HCl	HCR-6000
Optimal Pore Volume to Breakthrough	0.46	0.42
Optimal Interstitial Velocity (cm/min)	1.97	0.49
$PV_{BT\text{-}opt}$ difference	8.7%	
$V_{i\text{-}opt}$ difference	75.1%	

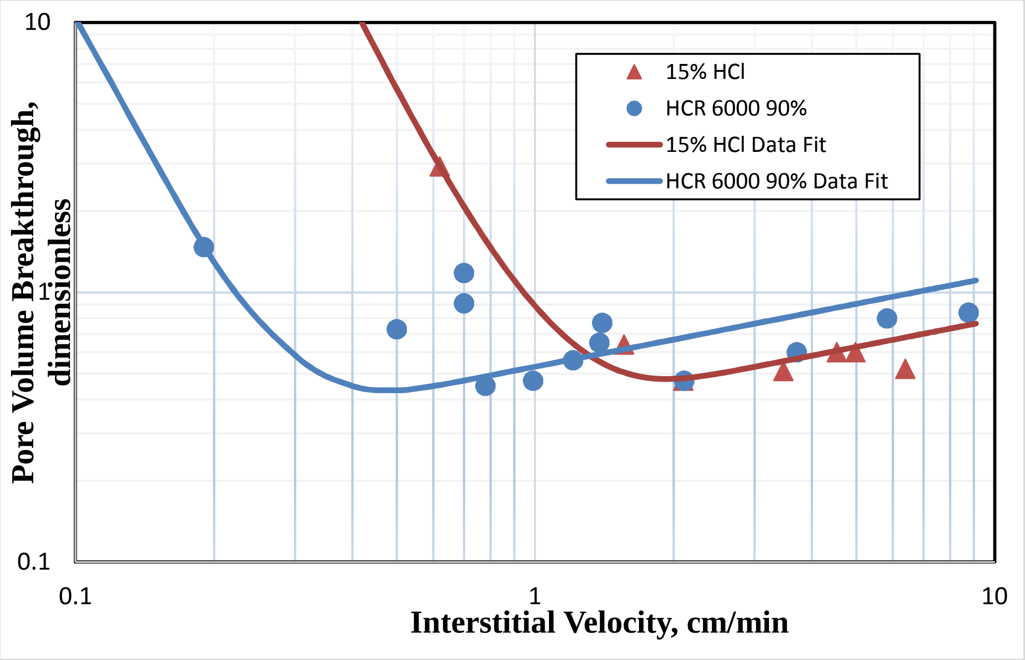

Figure 29. HCR-6000 and 15% HCl acid flux curves

The two curves shown in Figure 29 a large difference in optimal values for interstitial velocity. Despite their optimal PV_{BT} at their optimal interstitial velocity values seem to be similar, at lower rates, around HCR-6000's optimal interstitial velocity, the PV_{BT} of 15% HCl is exponentially higher than that of HCR-6000. It can be concluded that HCR-6000 performance is significantly superior at interstitial velocities lower than about 1.3cm/min. Some of the resulting core images and CT scanned wormhole structures are shown in Figure 30. The rest of the images can be found in Appendix A.

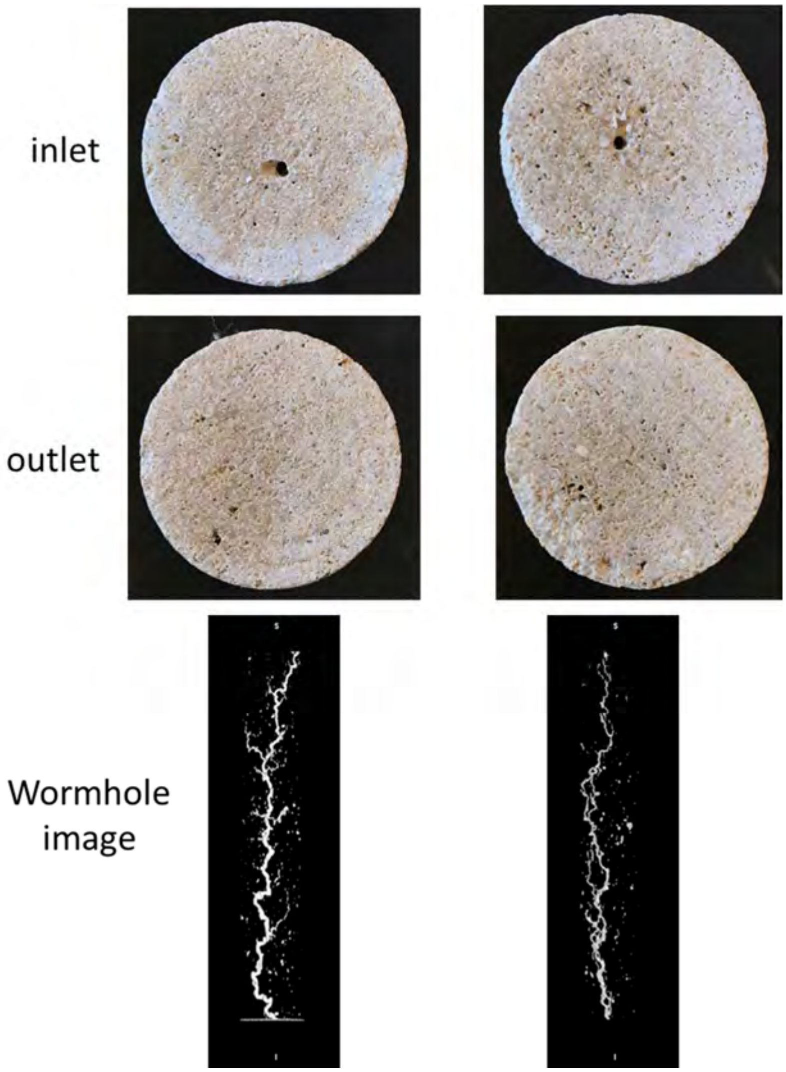

Figure 30. HCR-6000 (right) and 15%HCl (left) core and wormhole images

As it can be seen in Figure 30, the wormhole generated with HCR-6000 shows skinnier diameter, which substantiates the result of lower PV_{BT} at same interstitial velocity. More images of the individual cores can be found in Appendix A.

4.1.3 HCR-7000 Core Flood Experiment Results

This section shows the matrix acidizing coreflood results of the HCR-7000 acid. Table 8 lists the core properties. The average porosity was 14%, and permeability was 20mD.

Table 8. HCR-7000 Core Properties

	Core#	Dry weight(g)	Wet weight(g)	Perm(mD)	Porosity
HCR-7000	IC111	500.6	532.5	5.45	14.0%
	IC108	497.4	531.2	13.53	15.0%
	IC112	498.5	530.3	7.97	14.0%
	IC109	497.0	529.8	17.82	14.0%
	LDA16	499.9	535.7	39.69	15.0%

The experimental results show that the optimal pore volume to breakthrough and optimal interstitial velocity were both lower than that of 15% HCl, as you can see in Table 9 and Figure 31.

Table 9. HCR-7000 Experimental Results

Core#	Acid injection rate (ml/min)	Interstitial Velocity (cm/min)	Pore Volume to Breakthrough	Perm(mD)
IC111	10	6.37	0.63	5.45
IC108	5	3.01	0.46	13.53
IC112	3	1.92	0.49	7.97
IC109	2	1.2	0.57	17.82
LDA16	1	0.57	2.11	39.69

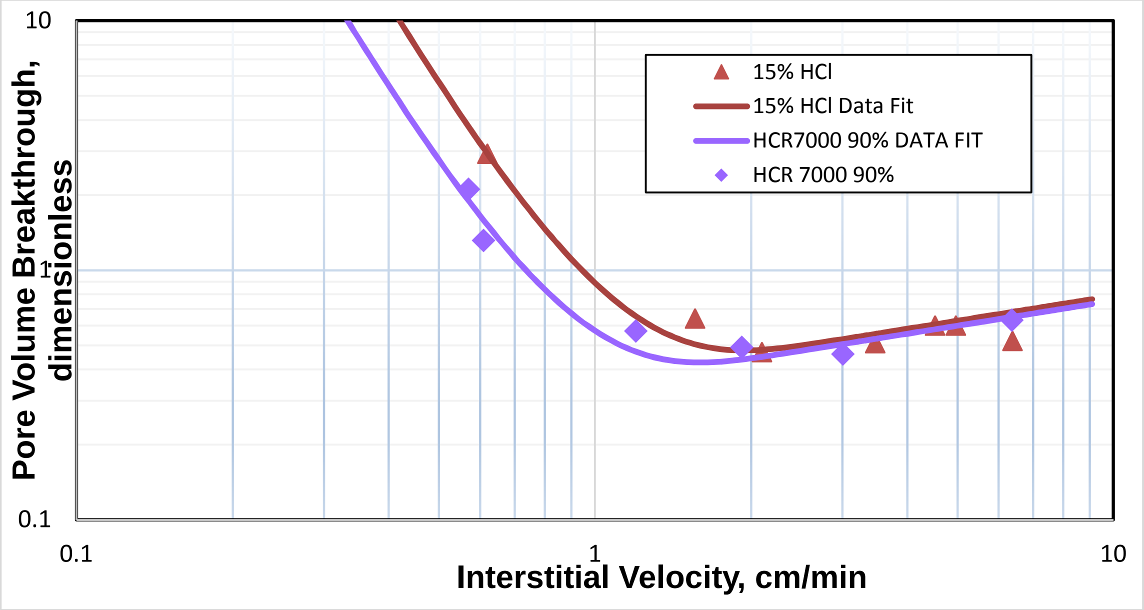

Figure 31. HCR-7000 and 15% HCl acid flux curves

From Figure 31, it seems that the curves overlap at interstitial velocities higher than 2 cm/min. However, at lower rates, the HCR-7000 shows higher efficiency with a lower PV_{BT} values. Below is the comparison of the optimal conditions for HCR-7000 and 15% HCl (Table 10).

Table 10. Optimal Condition Comparison between 15% HCl and HCR-7000

Optimal Condition		
	15% HCl	HCR 7000
$PV_{BT\text{-}opt}$	0.46	0.41
$V_{i\text{-}opt}$	1.97	1.62
$PV_{BT\text{-}opt}$ difference	11%	
$V_{i\text{-}opt}$ difference	18%	

Figure 32 displays a CT scan image of the HCR-7000 experimental core.

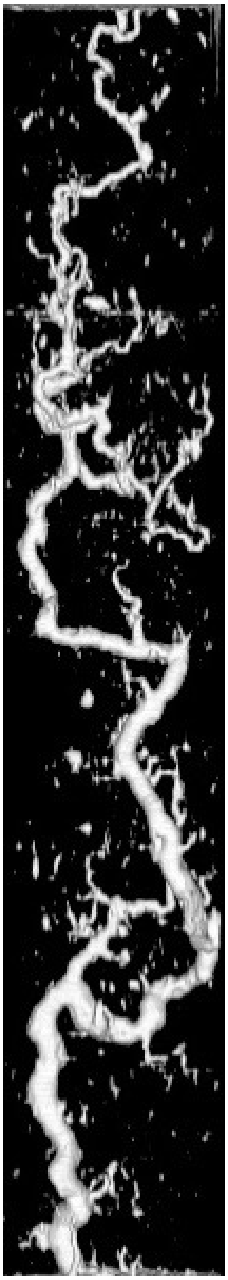

Figure 32. LDA16 wormhole structure

More detailed wormhole CT scan images and core inlet and outlet images are found in Appendix A.

4.1.4 HCR-8000 Core Flood Experiment Results

This section shows the coreflood experimental results of HCR-8000 acid. The same experimental procedure was followed as previous experiments. The core properties are shown in Table 11. The average porosity of the cores was 14%, and permeability was 22mD.

Table 11. HCR-8000 Core Properties

	Core#	Dry weight(g)	Wet weight(g)	Perm(mD)	Porosity
90% HCR 8000	IC102	500.5	531.6	2.77	13.0%
	IC101	500.1	531.4	5.61	14.0%
	IC201	499.2	530.9	39.69	14.0%
	IC202	499.2	531.6	38.81	14.0%

The core flood results of HCR-8000 are found in Table 12 and the optimal conditions are shown in Table 13. The data points and curve-fit wormhole efficiency plot are shown in Figure 33.

Table 12. HCR-8000 Experimental Results

Core#	Acid injection rate (ml/min)	Interstitial Velocity (cm/min)	Pore Volume to Breakthrough	Perm(mD)
IC102	5	3.27	0.61	2.77
IC101	2	1.3	0.58	5.61
IC201	1	0.64	0.78	39.69
IC202	0.8	0.5	1.34	38.81

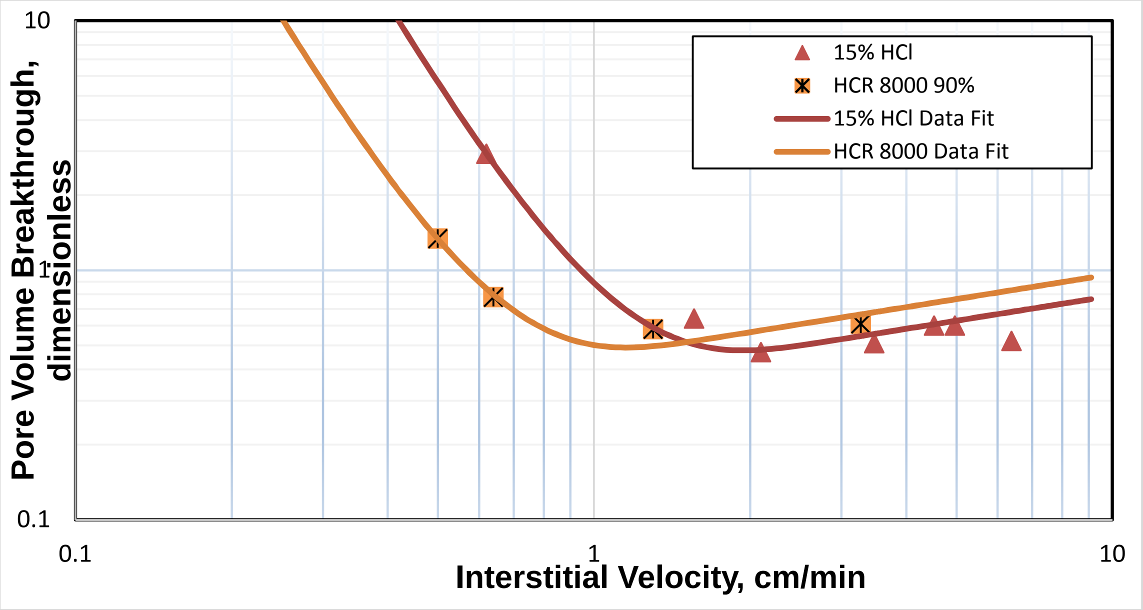

Figure 33. HCR-8000 and 15% HCl acid flux curves

Table 13. Optimal Condition Comparison between 15% HCl and HCR-8000

Optimal Condition		
	15% HCl	HCR-8000
$PV_{BT\text{-}opt}$	0.46	0.47
$V_{i\text{-}opt}$	1.97	1.17
$PV_{BT\text{-}opt}$ difference	-2%	
$V_{i\text{-}opt}$ difference	40%	

Overall, the HCR-8000 showed similar advantage as HCR-6000 and HCR-7000, except that its optimal pore volume to break through value was just a bit higher at its optimal interstitial velocity. It can be concluded from the wormhole efficiency plot in Figure 33 that when interstitial velocity is higher than 1.5 cm/min, 15% HCl is more efficient because it has lower PV_{BT}, but at lower injection rate, HCR-8000 is more efficient compared to 15% HCl. Appendix A includes the wormhole images and core images after the matrix acidizing experiments.

4.1.5 Comprehensive Acid Comparison

Figure 34 below contains all four of the acid flux curves conducted for this study. From this figure, it can be concluded that HCR-6000 is the most effective acid system at lower interstitial velocity conditions, followed by HCR-8000 and HCR-7000. Table 14 contains the optimal conditions for all acids for comparison.

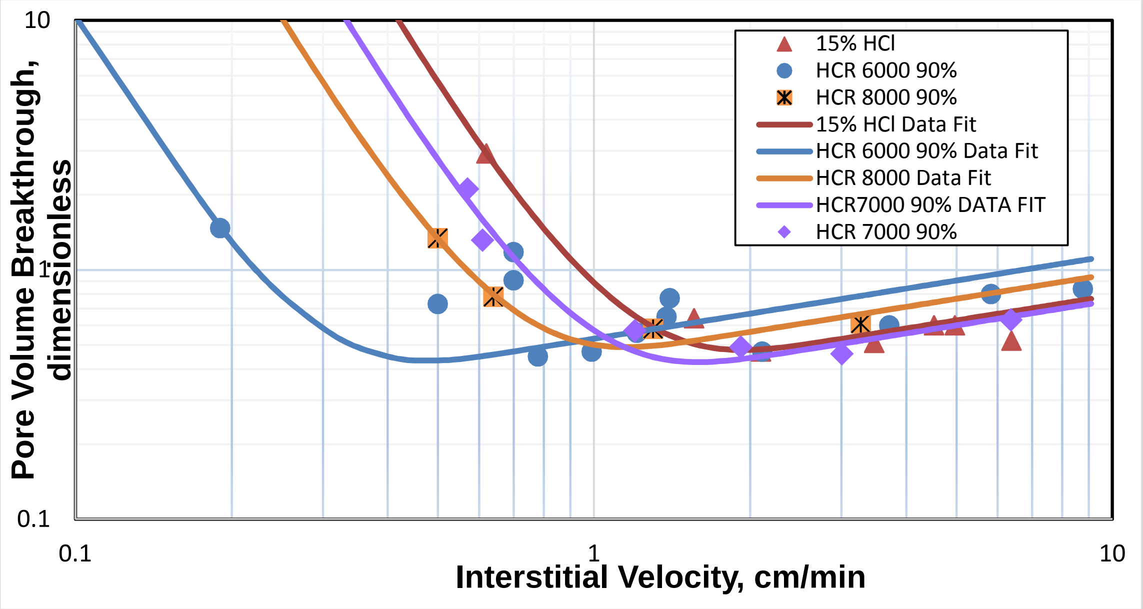

Figure 34. Comprehensive Acid Flux Curves

Table 14. Optimal Condition Comparison for All Acids

Optimal Condition				
	15% HCl	HCR-6000	HCR-7000	HCR-8000
$PV_{BT\text{-}opt}$	0.46	0.42	0.41	0.47
$V_{i\text{-}opt}$	1.97	0.49	1.62	1.17
$PV_{BT\text{-}opt}$ advantage to HCl	-	9%	11%	-2%
$V_{i\text{-}opt}$ advantage to HCl	-	75%	18%	41%

4.2 Evaluation of Acid System for Productivity

To understand and visualize the performance of the acids, the resulting data from the experiments were analyzed. The analysis follows the Buijse-Glasbergen model of wormhole propagation. The wormhole propagation velocity, v_{wh}, is

$$v_{wh} = \left(\frac{v_i}{PV_{bt,opt}}\right) \times \left(\frac{v_i}{v_{i,iopt}}\right)^{-\gamma} \times \left\{1 - \exp\left[-4\left(\frac{v_i}{v_{i,opt}}\right)^2\right]\right\}^2 \tag{4.7}$$

For each of the acid system, the $PV_{BT,opt}$ and $v_{i,opt}$ values were changed based on experimental observation and wormhole length is calculated. The wormhole length at each time step was calculated by simply computing how much wormhole has increased by multiplying the wormhole propagation velocity to the time step (in this case 0.1 min) and adding to the wormhole length at previous time step.

$$r_{wh,i} = r_{wh,i-1} + v_{wh,i} * 0.1 \tag{4.8}$$

The final wormhole length is then used to calculate and equivalent skin factor for acid stimulation outcome,

$$s = -\ln\left(\frac{r_{wh}}{r_w}\right) \tag{4.9}$$

This skin factor evaluates the effectiveness of well stimulation. Assuming that there exists a damage skin factor s_d after acidizing, the well productivity in a dimensionless form is,

$$J_D = \frac{1}{\ln\left(\frac{r_e}{r_w}\right)+s} \quad \text{(4.10)}$$

and the productivity improvement is,

$$\frac{J_{D_S}}{J_D} = \frac{\ln\left(\frac{r_e}{r_w}\right)+s_a}{\ln\left(\frac{r_e}{r_w}\right)+s_d} \quad \text{(4.11)}$$

The input data used in the evaluation is listed in Table 15.

Table 15. Assumed Values for Productivity Calculation

Injection Rate	2 BPM
Porosity	14%
Wellbore Thickness	1000ft
Initial Wellbore Radius	0.4ft
Reservoir Radius	798ft
Wellbore Pressure	3000psi
Reservoir Pressure	5000psi
Permeability	30mD
Fluid Viscosity	1cp
Formation Volume Factor	1.117

Below are the sample calculations with a 15% HCl data point for the productivity estimation.

The wormhole velocity (v_{wh}) is estimated as following:

$$v_i = \frac{Q*5.615}{2*\pi*h*r_w*\phi}\left[\frac{ft}{min}\right] \quad \text{(4.12)}$$

$$v_i = \frac{2*5.615}{2*\pi*1000*0.4*0.14} = 0.03\frac{ft}{min}\ or\ 1.0\frac{cm}{min} \tag{4.13}$$

$$v_{wh} = \left(\frac{v_i}{PV_{bt,opt}}\right) \times \left(\frac{v_i}{v_{i,iopt}}\right)^{-\gamma} \times \left\{1 - \exp\left[-4\left(\frac{v_i}{v_{i,opt}}\right)^2\right]\right\}^2 \tag{4.14}$$

$$v_{wh} = \left(\frac{1.0}{5.7}\right) \times \left(\frac{1.0}{0.5}\right)^{-\frac{1}{3}} \times \left\{1 - \exp\left[-4\left(\frac{1.0}{0.5}\right)^2\right]\right\}^2 = 0.14\frac{cm}{min}\,or\ 0.004\frac{ft}{min} \tag{4.15}$$

The wormhole length (r_{wh}) is calculated as following:

$$r_{wh,i} = r_{wh,i-1} + v_{wh,i} * \Delta t \tag{4.16}$$

$$r_{wh,1} = 0.4 + 0.004 * 0.1 = 0.4004\ ft \tag{4.17}$$

$$r_{wh,2} = 0.4004 + 0.004 * 0.1 = 0.4008\ ft \tag{4.18}$$

The skin (s) is calculated as following:

$$s = -\ln\left(\frac{r_{wh}}{r_w}\right) \tag{4.19}$$

$$s_a = -\ln\left(\frac{0.4004}{0.4}\right) = -0.0011\ after\ 0.1\ min \tag{4.20}$$

where s_a is the stimulated skin. The productivity index (J_D) is calculated as following:

$$J_D = \frac{1}{\ln\left(\frac{r_e}{r_w}\right)+s} = \frac{1}{\ln\left(\frac{r_e}{{r'}_w}\right)} \tag{4.21}$$

$$r'_w = r_w * e^{-s} \tag{4.22}$$

$$r'_w = 0.4 * e^{-(-0.0011)} = 0.4005ft \tag{4.23}$$

$$J_{D_s} = \frac{1}{\ln\left(\frac{798}{0.4005}\right)} = 0.131626 \qquad (4.24)$$

where r'$_w$ is the effective wellbore radius and J_{Ds} is the stimulated productivity index.

The productivity index improvement (J_{Ds}/J_D) is calculated as following:

$$\frac{J_{D_s}}{J_D} = \frac{\ln\left(\frac{r_e}{r_w}\right)+s_a}{\ln\left(\frac{r_e}{r_w}\right)+s_d} \qquad (4.25)$$

where s_d is the damage skin. If damage skin is 10, ,

$$r_w' = 0.4 * e^{-10} = 0.0000182\ ft \qquad (4.26)$$

$$J_D = \frac{1}{\ln\left(\frac{798}{0.0000182}\right)} = 0.057 \qquad (4.27)$$

$$\frac{J_{D_s}}{J_D} = \frac{0.132}{0.057} = 2.3 \qquad (4.28)$$

which shows that the productivity of the stimulated case is 2.3 times higher than that of damaged case. If damage skin is 0,

$$r_w' = 0.4 * e^{-0} = 0.4\ ft \qquad (4.29)$$

$$J_D = \frac{1}{\ln\left(\frac{798}{0.4}\right)} = 0.131607 \qquad (4.30)$$

$$\frac{J_{D_s}}{J_D} = \frac{0.131626}{0.131607} = 1.0015 \qquad (4.31)$$

which shows that the productivity of the stimulated case is just about the same, as expected with zero damage skin.

4.2.1 HCR-6000 Buijse-Glasbergen Performance Modeling Results

Figure 35 shows HCR-6000 and 15% HCl acid flux curves on the same chart. It is obvious that at a low interstitial velocity, the pore volume to breakthrough for 15% HCl increases exponentially, which means that 15% HCl is very inefficient compared to HCR-6000 at these rates. Two interstitial velocity rates were picked to give a reasonable comparison between the performance of HCR-6000 and 15% HCl. Table 16 shows the modeling conditions for the acids.

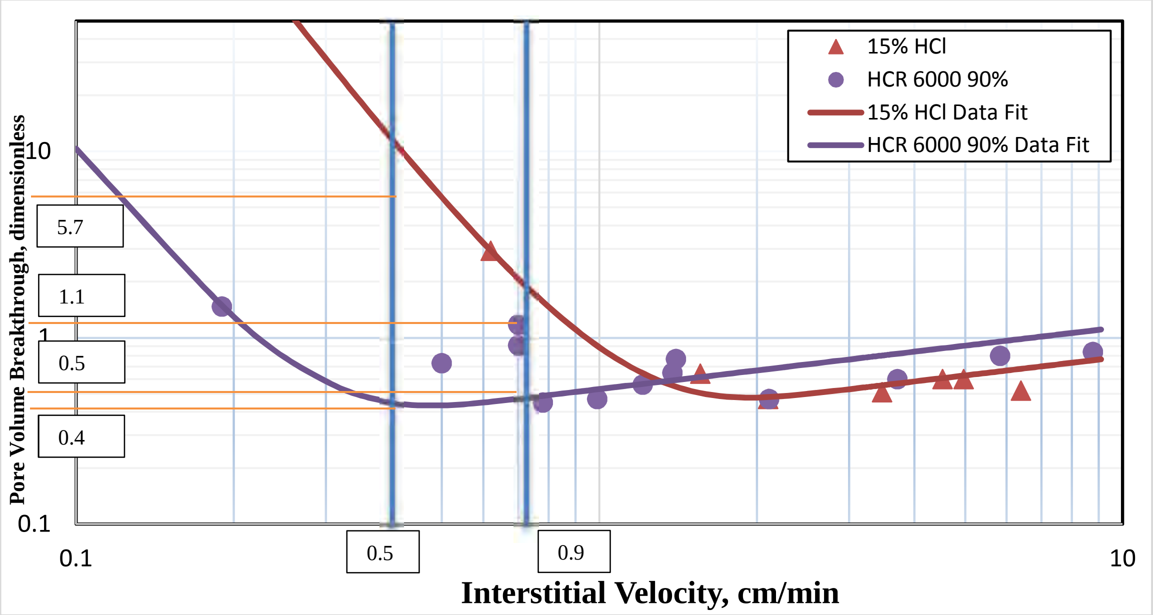

Figure 35. Acid flux curves for HCR-6000 and 15% HCl

Table 16. Modeling Conditions for HCR-6000 and 15% HCl

Modeling Conditions			
		15% HCl	HCR 6000
Case 1	$v_{i,1}$	0.5	0.5
	$PV_{BT,1}$	5.7	0.4
Case 2	$v_{i,2}$	0.9	0.9
	$PV_{BT,2}$	1.1	0.5

The interstitial velocities compared had enough differences in pore volume to breakthrough values to illustrate HCR-6000's superior performance at low acid injection rates. Below (Figures 36 through 40) are the graphs for easier understanding of the difference in their performance.

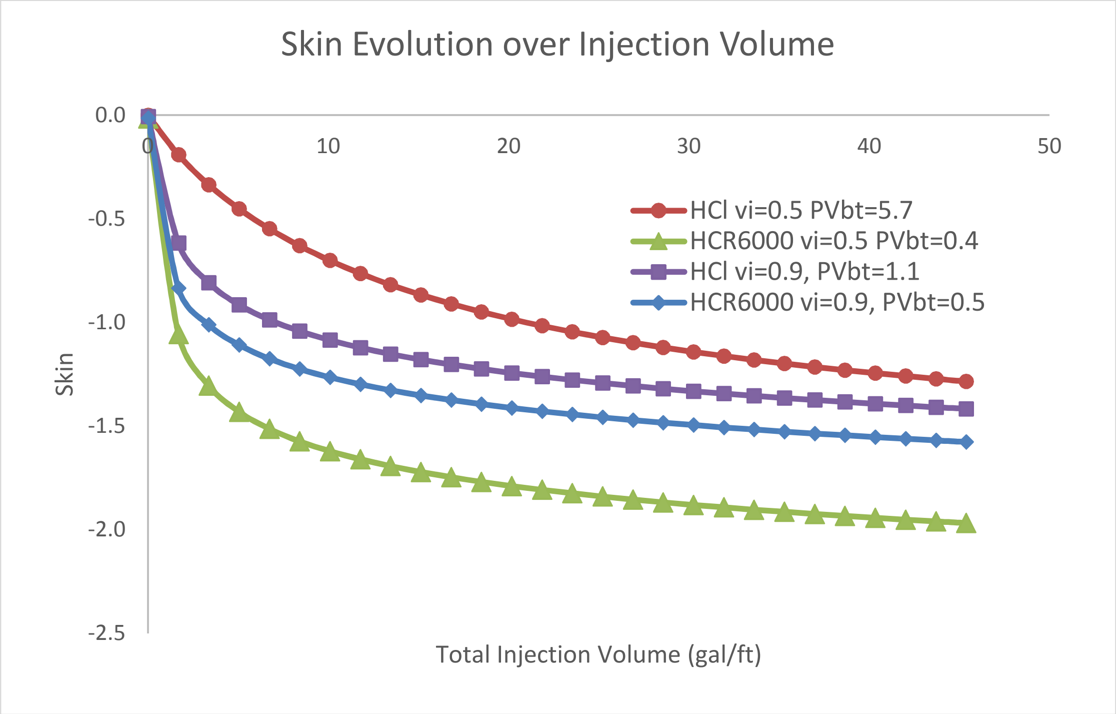

Figure 36. Skin evolution over injection volume HCR-6000

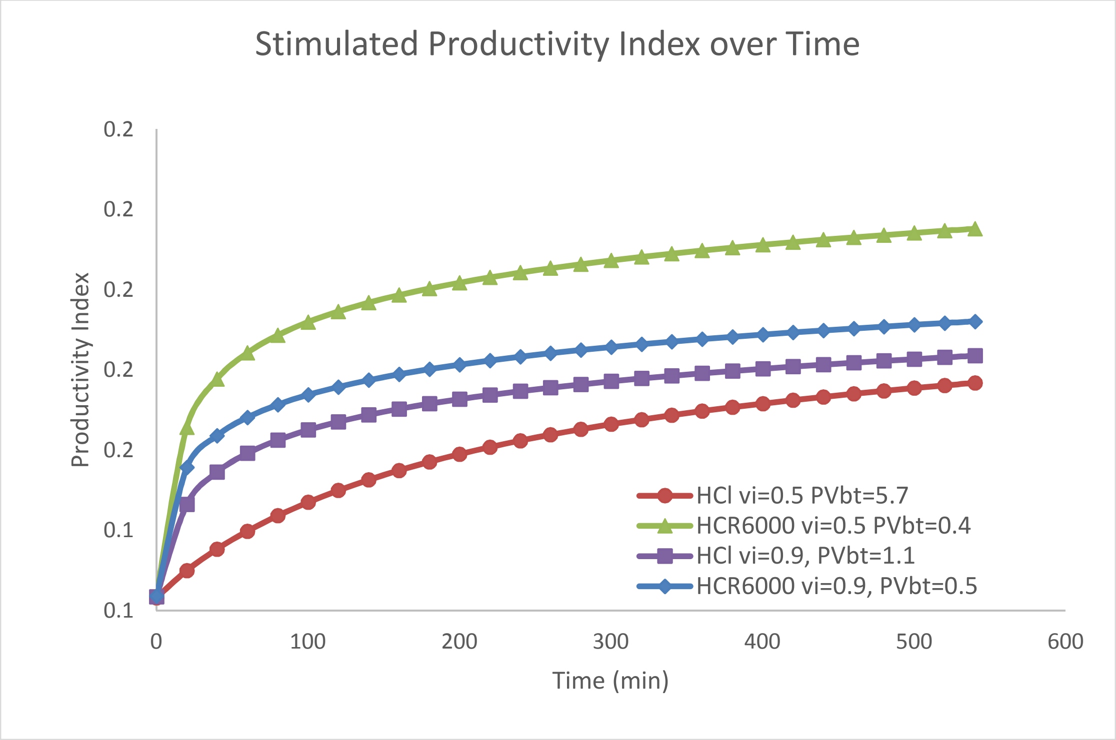

Figure 37. Stimulated productivity index over time HCR-6000

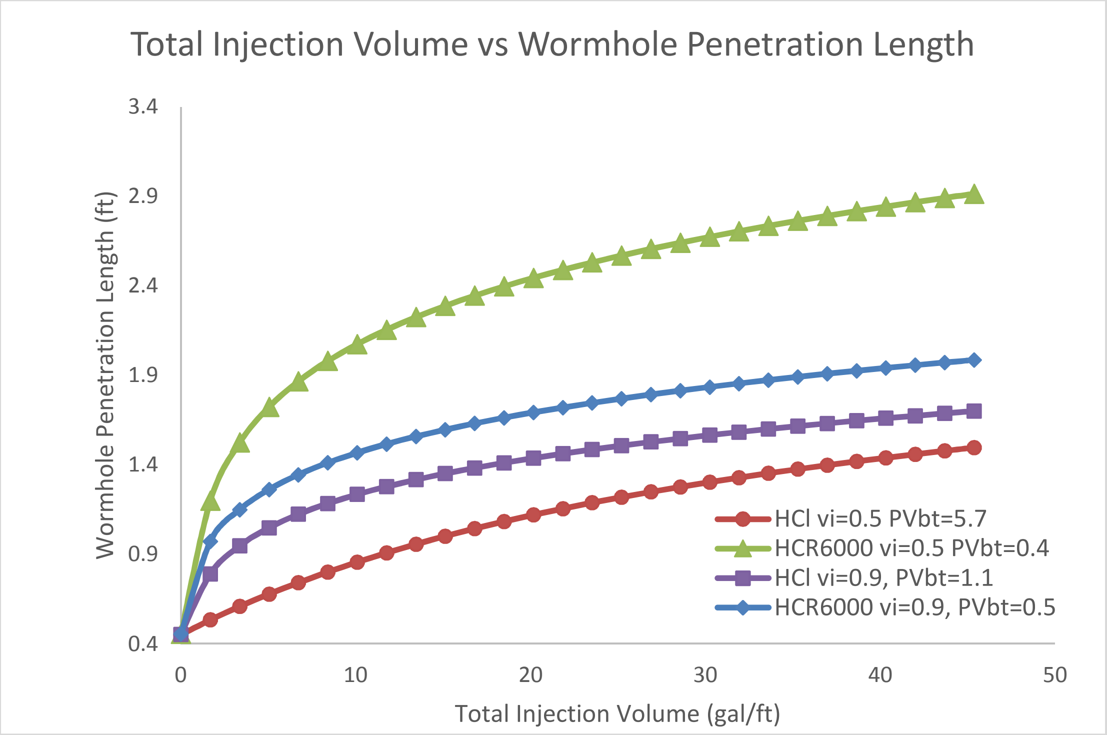

Figure 38. Wormhole penetration length over total injection volume HCR-6000

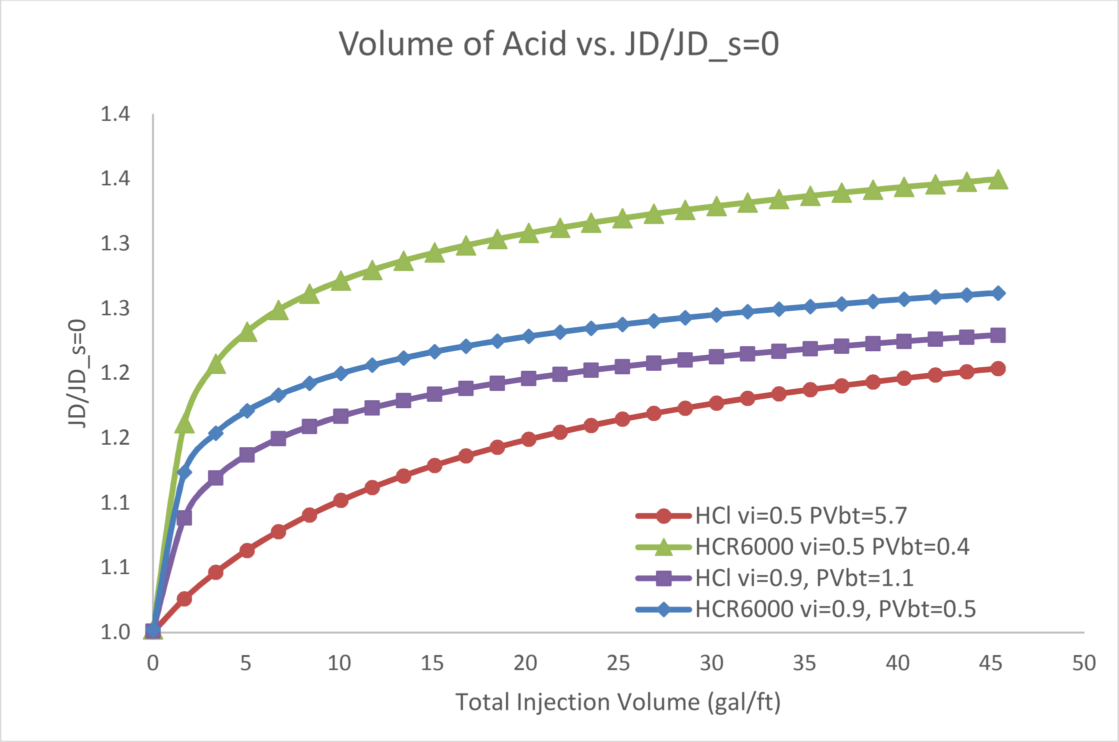

Figure 39. Productivity index comparison at 0 skin HCR-6000

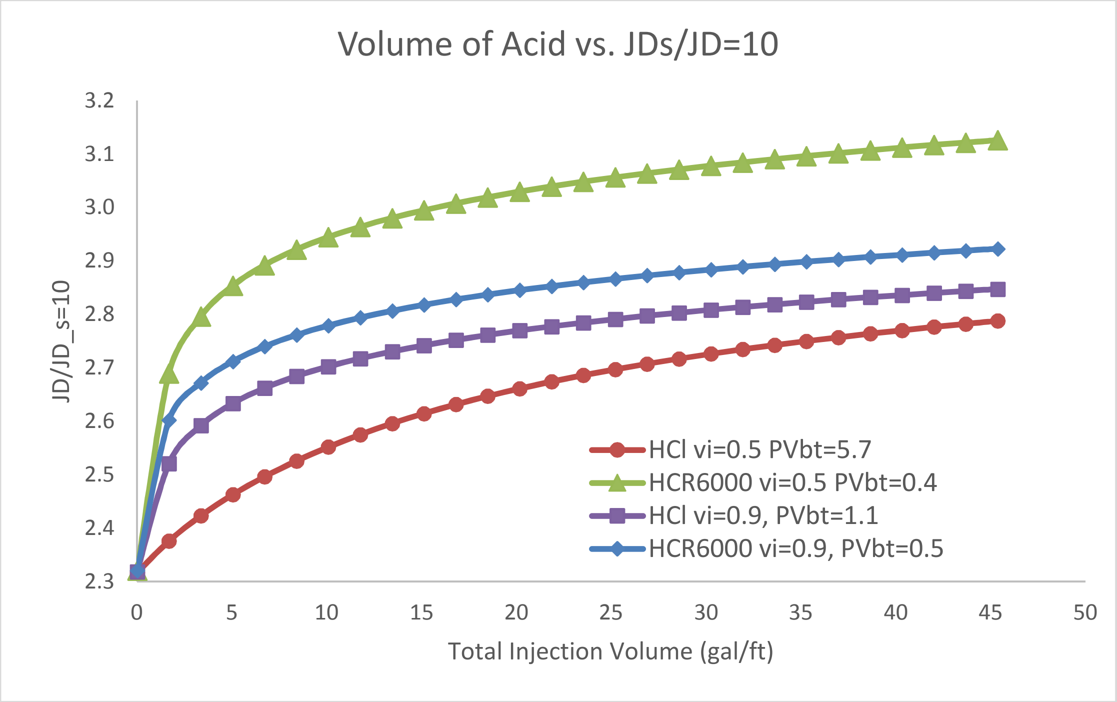

Figure 40. Productivity index comparison at 10 skin HCR-6000

From these graphs, it is apparent that HCR-6000's performance is superior. One point to note is that 15% HCl's performance is slightly better at interstitial velocities at or above 1.5 cm/min, and the difference in acid efficiency within 0.5 pore volume, whereas if acid efficiency at interstitial velocity of 0.2cm/min were to be compared, the 15% HCl is much worse at pore volume difference of more than 100, and the resulting graphs would show even more drastic difference.

4.2.2 HCR-7000 Buijse-Glasbergen Performance Modeling Results

In order to compare the performance of HCR-7000 and 15% HCl, some modeling work was done at two interstitial velocity values shown in Figure 41.

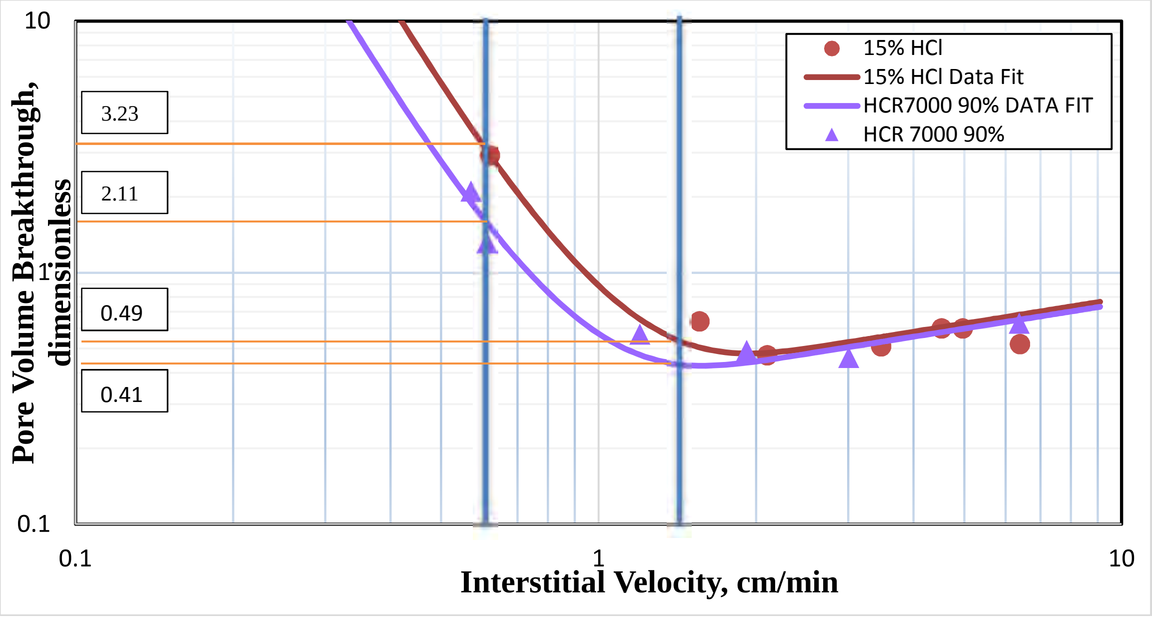

Figure 41. Acid flux curves for HCR-7000 and 15% HCl

To compare their performance, v_i near HCR-7000's optimal condition and at a lower condition were modeled. Two vertical lines in Figure 41 indicate the v_i values chosen for comparison. Table 17 contains the corresponding PV_{BT} values at selected v_i.

Table 17. Modeling Conditions for HCR-7000 and 15% HCl

Modeling Conditions			
		15% HCl	HCR 7000
Case 1	$\mathbf{v_{i,1}}$	**1.6**	**1.6**
	$PV_{BT,1}$	0.49	0.41
Case 2	$\mathbf{v_{i,2}}$	**0.6**	**0.6**
	$PV_{BT,2}$	3.23	2.11

Shown below in Figures 42 through 46 are the graphs generated with these conditions. The four curves in each graph represent 15% HCl and HCR-7000 performance at two different interstitial velocities.

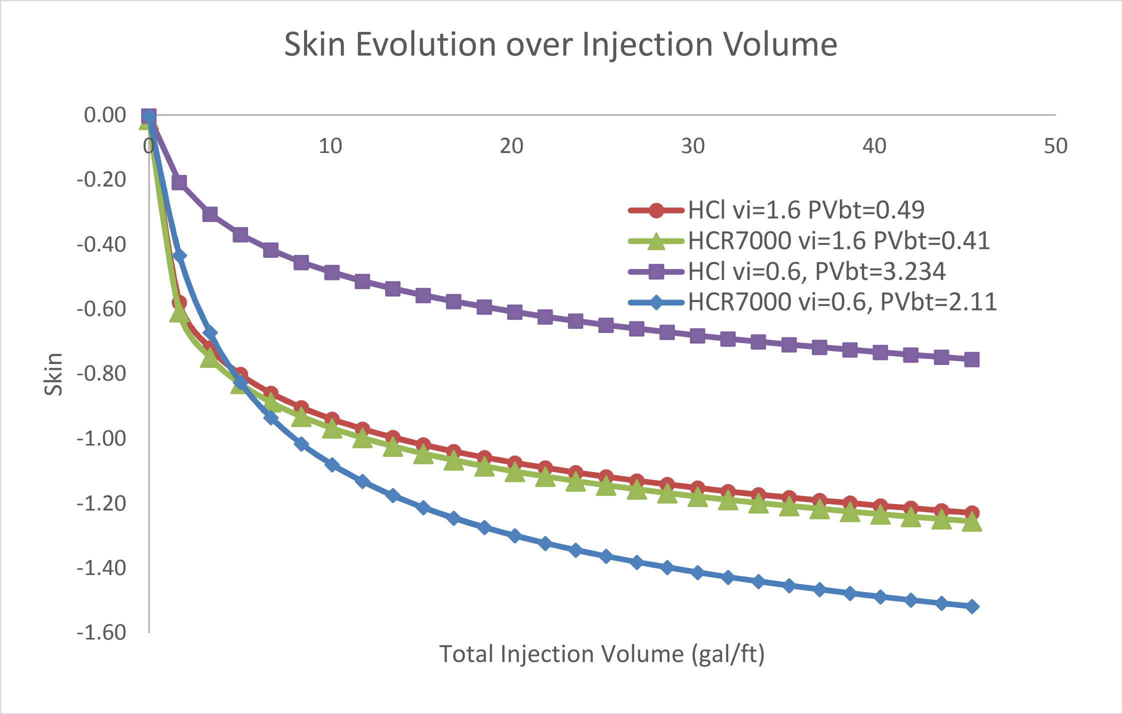

Figure 42. Skin evolution over injection volume HCR-7000

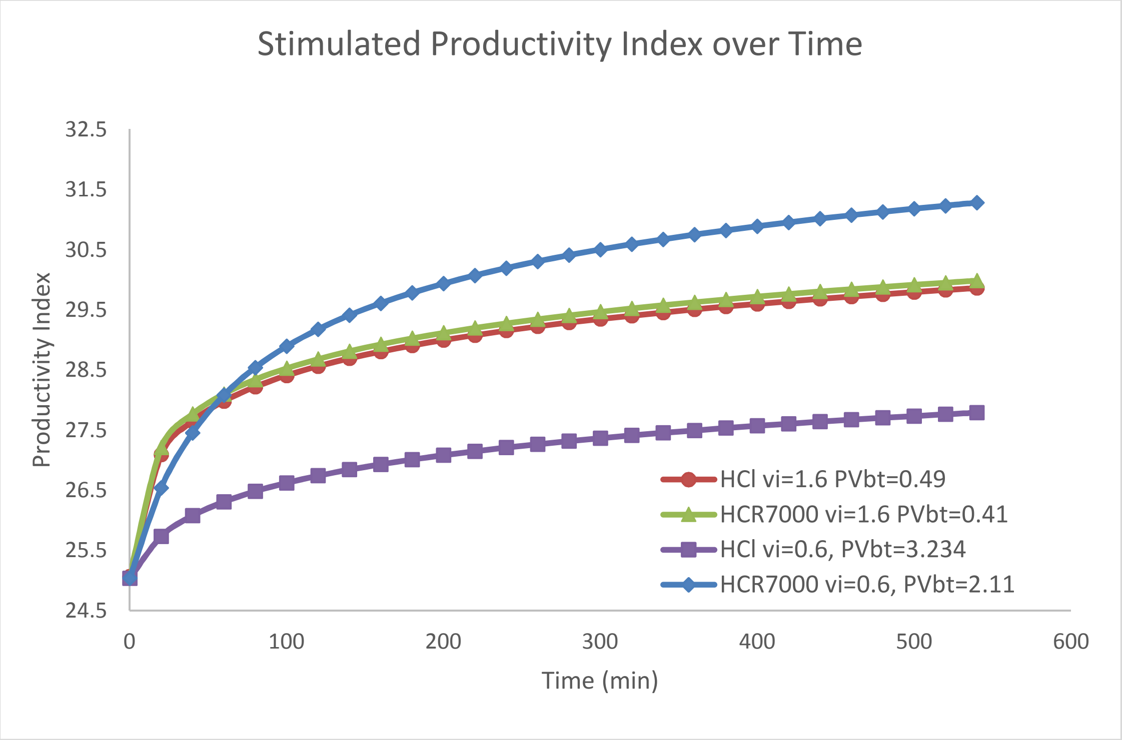

Figure 43. Stimulated productivity index over time HCR-7000

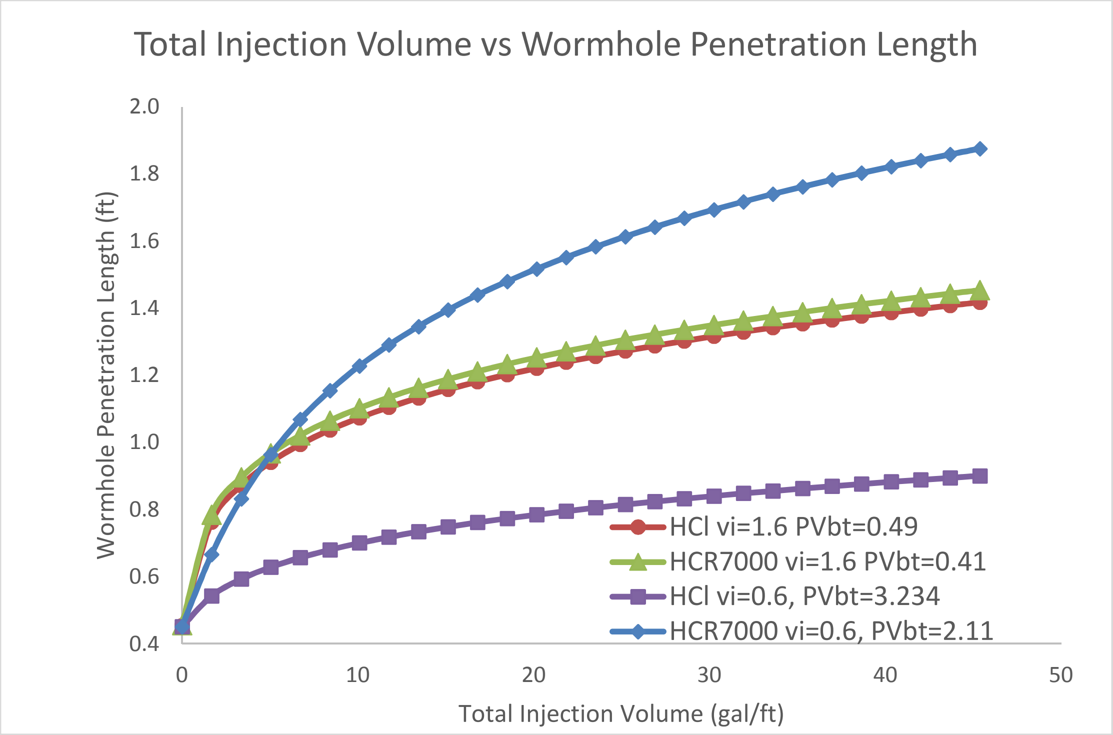

Figure 44. Wormhole penetration length over total injection volume HCR-7000

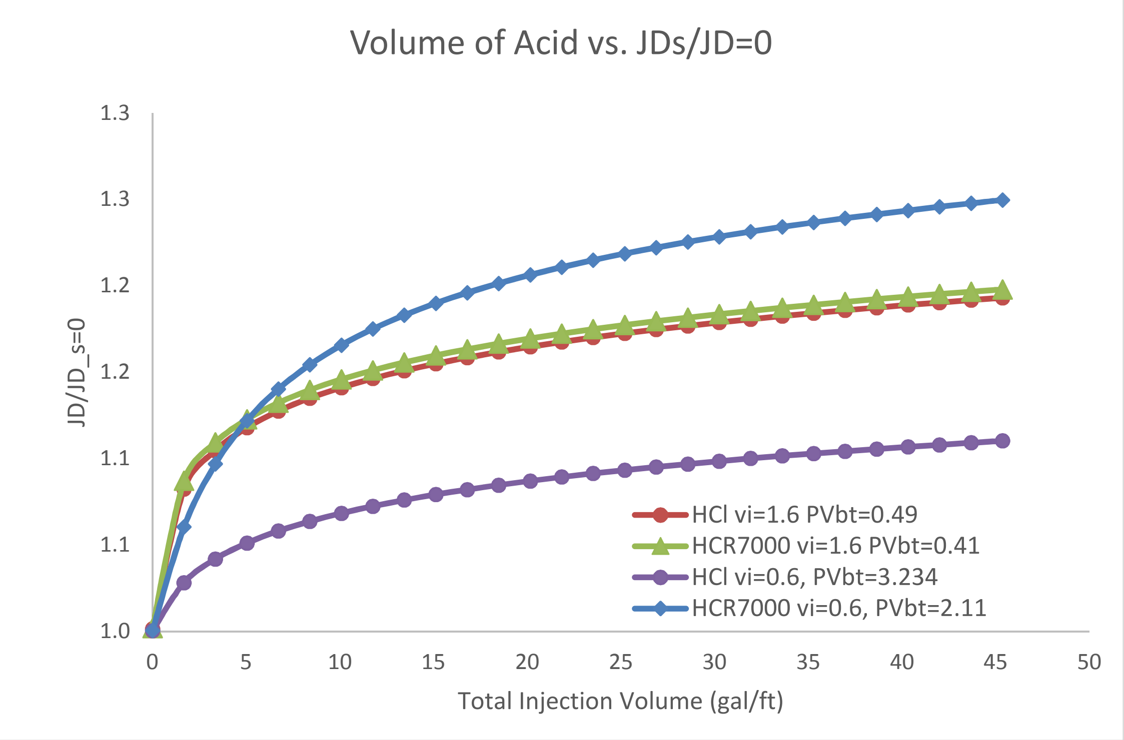

Figure 45. Productivity index comparison at 0 skin HCR-7000

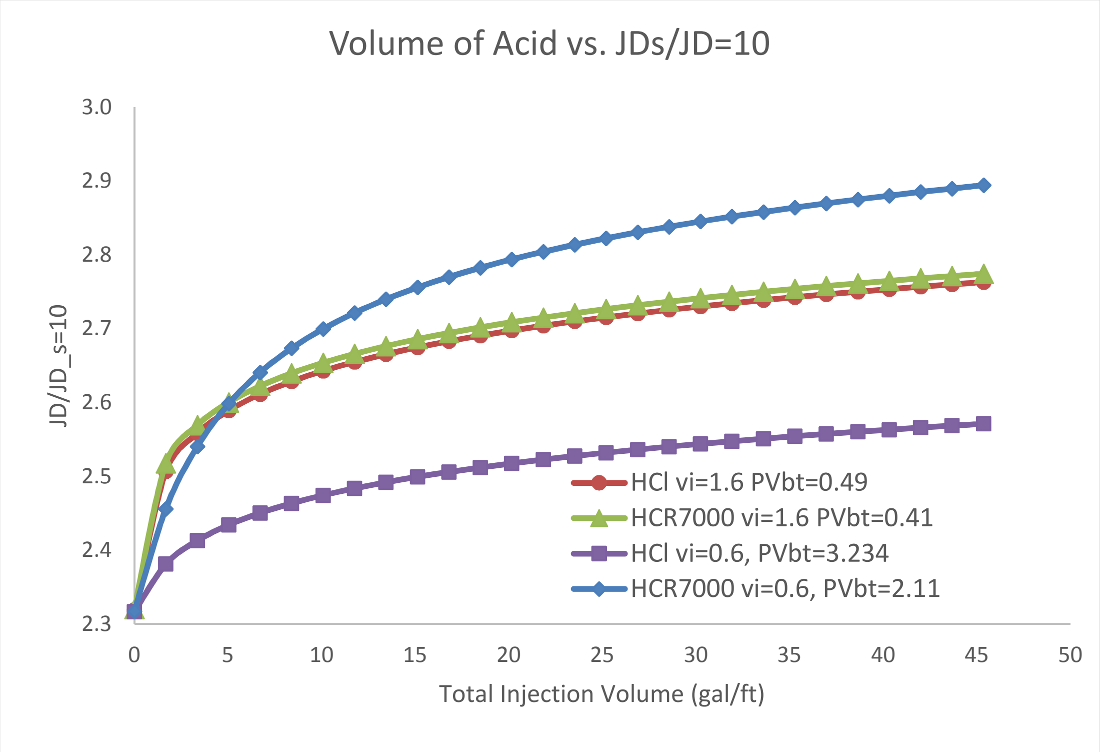

Figure 46. Productivity index comparison at 10 skin HCR-7000

As shown above in the comparisons, HCR-7000 shows better performance at low interstitial velocity compared to 15% HCl. This means that if the acid stimulation operation has a limitation for pumping rate below 15% HCl's optimum interstitial velocity, HCR-7000 has definite advantage compared to 15% HCl. At higher than 15% HCl's interstitial velocity, the performance of these acids are similar.

4.2.3 HCR-8000 Buijse-Glasbergen Performance Modeling Results

In order to compare the performance of HCR-8000 and 15% HCl, some modeling work was done at two interstitial velocity values. To compare their performance, two v_i values were selected. As seen in Figure 47, the two vertical lines in indicate the v_i values chosen for comparison. Table 18 contains the corresponding PV_{BT} values at the selected v_i.

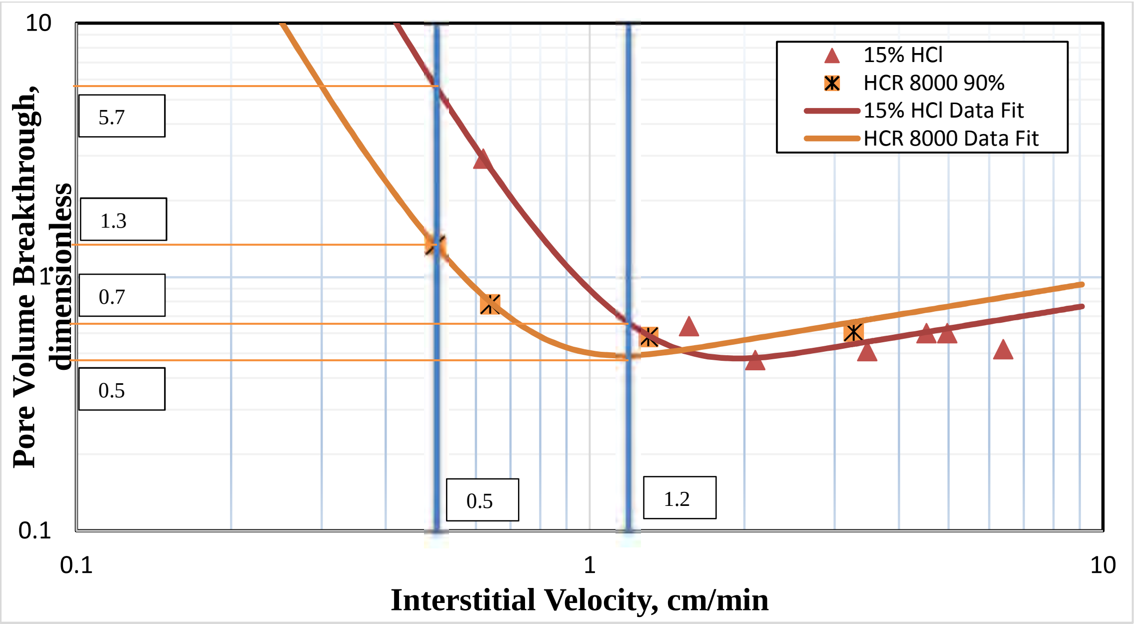

Figure 47. Acid flux curves for HCR-8000 and 15% HCl

Table 18. Modeling Conditions for HCR-8000 and 15% HCl

Modeling Conditions			
		HCl	HCR-8000
Case 1	$\mathbf{v_{i,1}}$	**0.5**	**0.5**
	$PV_{BT,1}$	5.7	1.3
Case 2	$\mathbf{v_{i,2}}$	**1.2**	**1.2**
	$PV_{BT,2}$	0.7	0.5

Shown below in Figures 48 through 52 are the graphs generated with these conditions. The four curves in each graph represent 15% HCl and HCR-8000 performance at two different interstitial velocities.

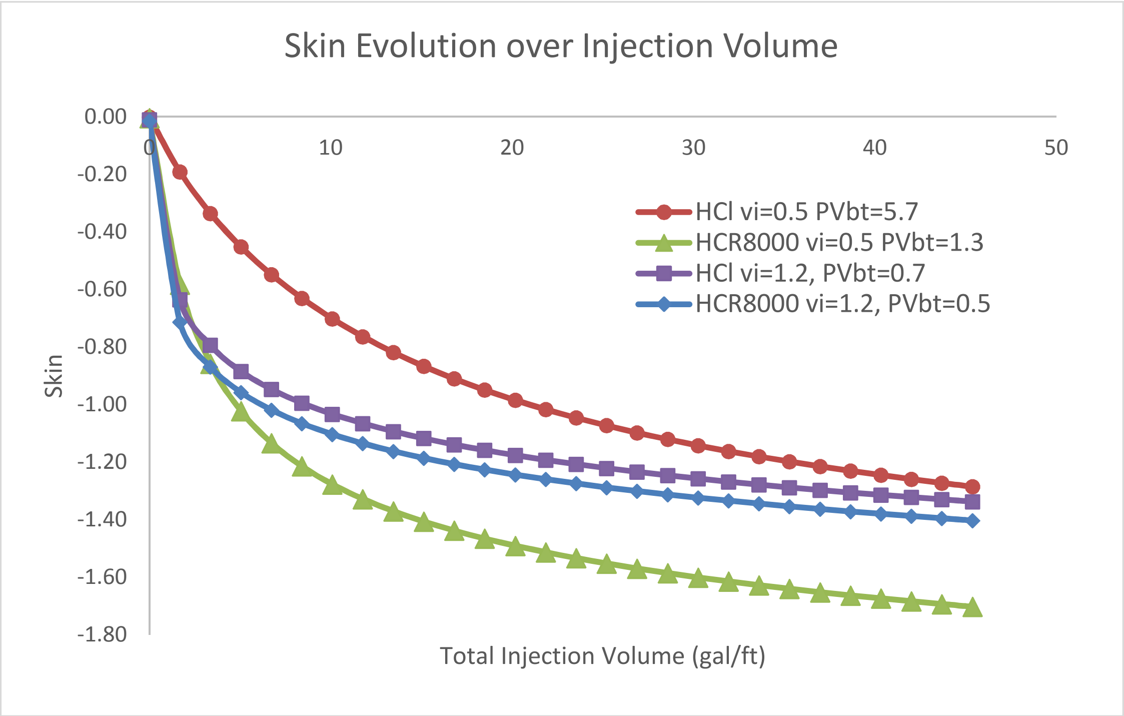

Figure 48. Skin evolution over injection volume HCR-8000

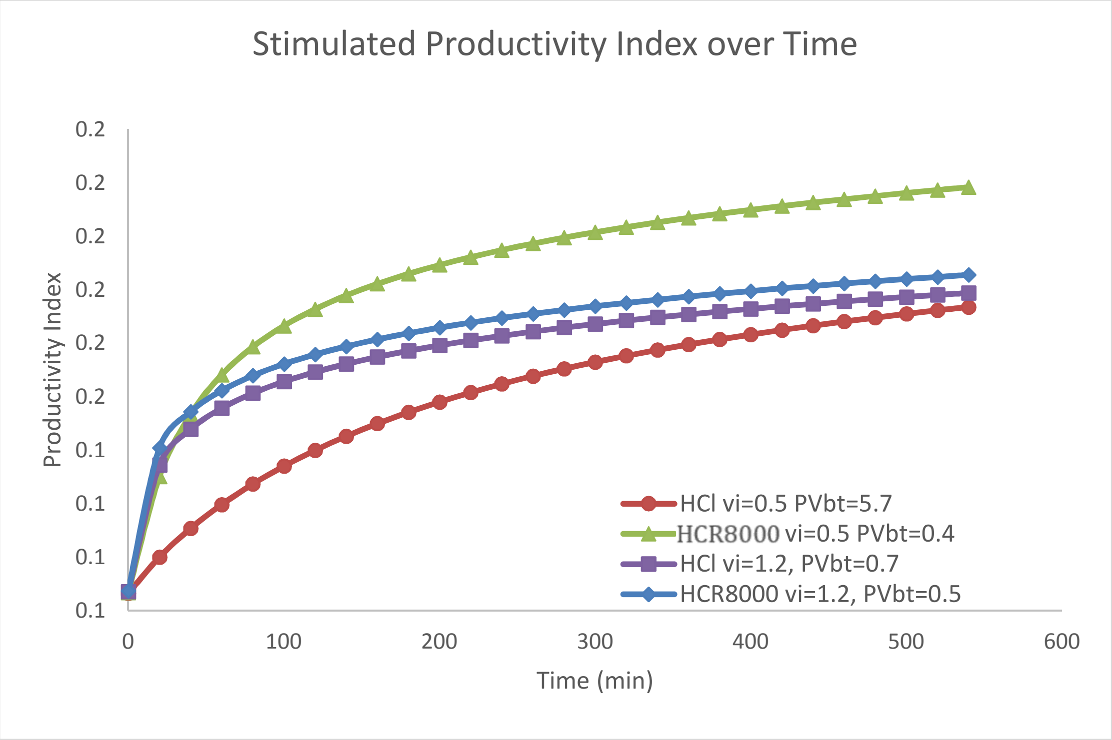

Figure 49. Stimulated productivity index over time HCR-8000

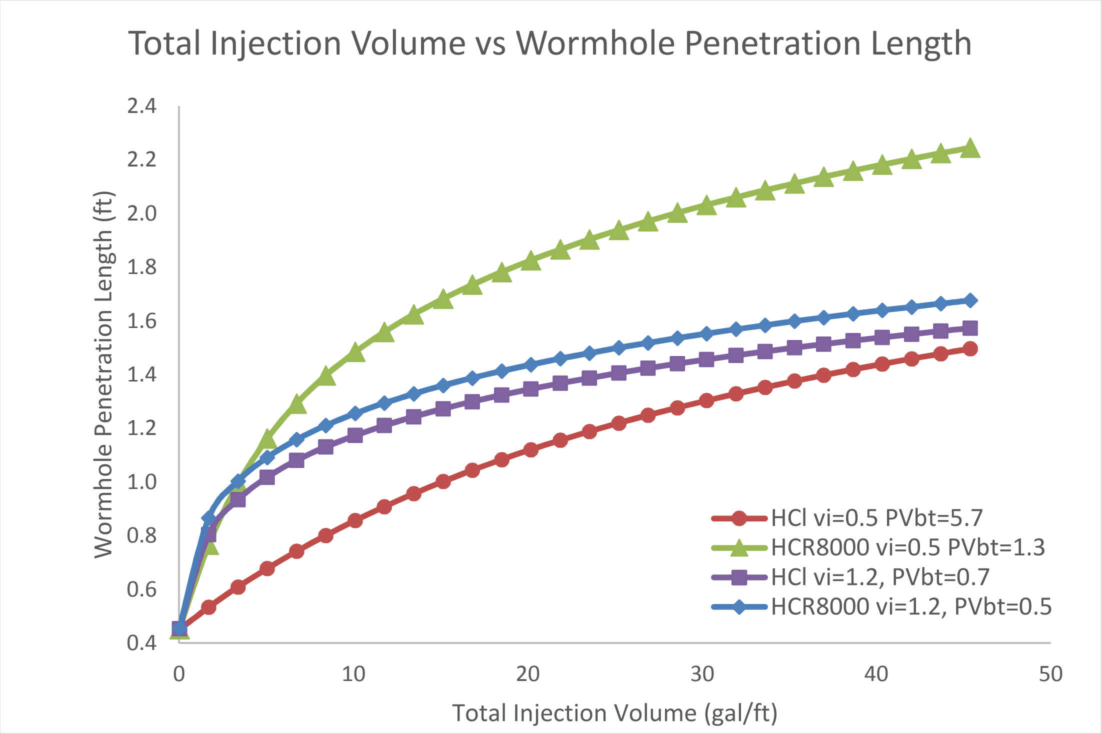

Figure 50. Wormhole penetration length over total injection volume HCR-8000

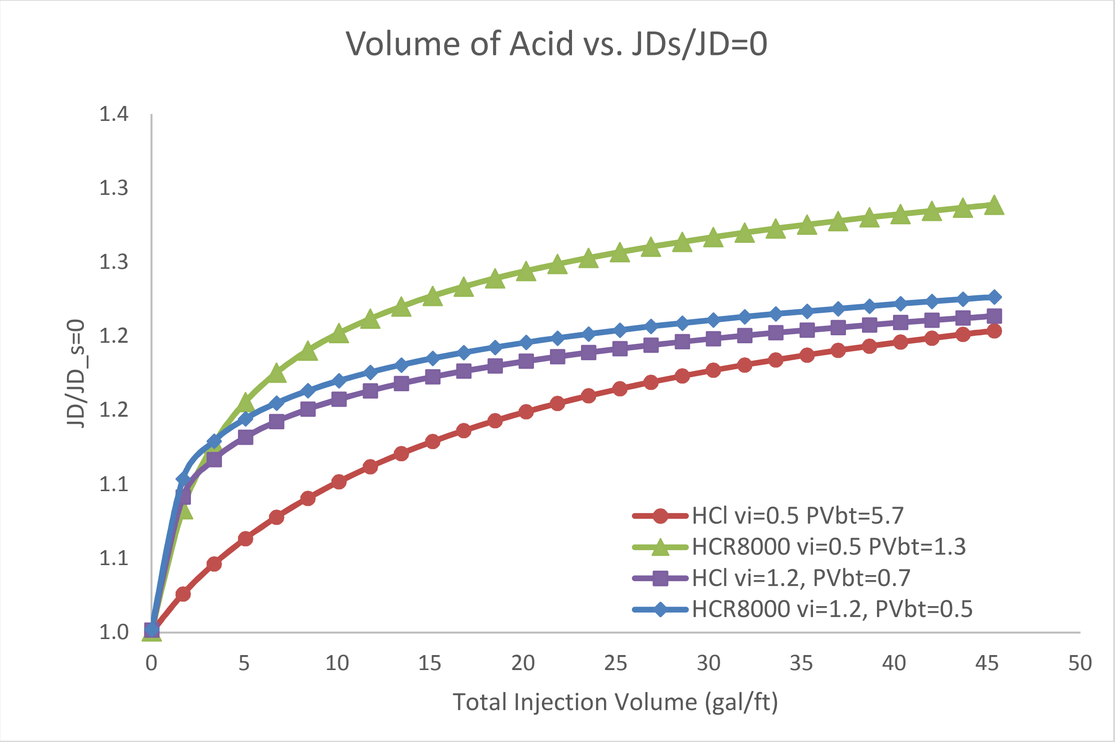

Figure 51. Productivity index comparison at 0 skin HCR-8000

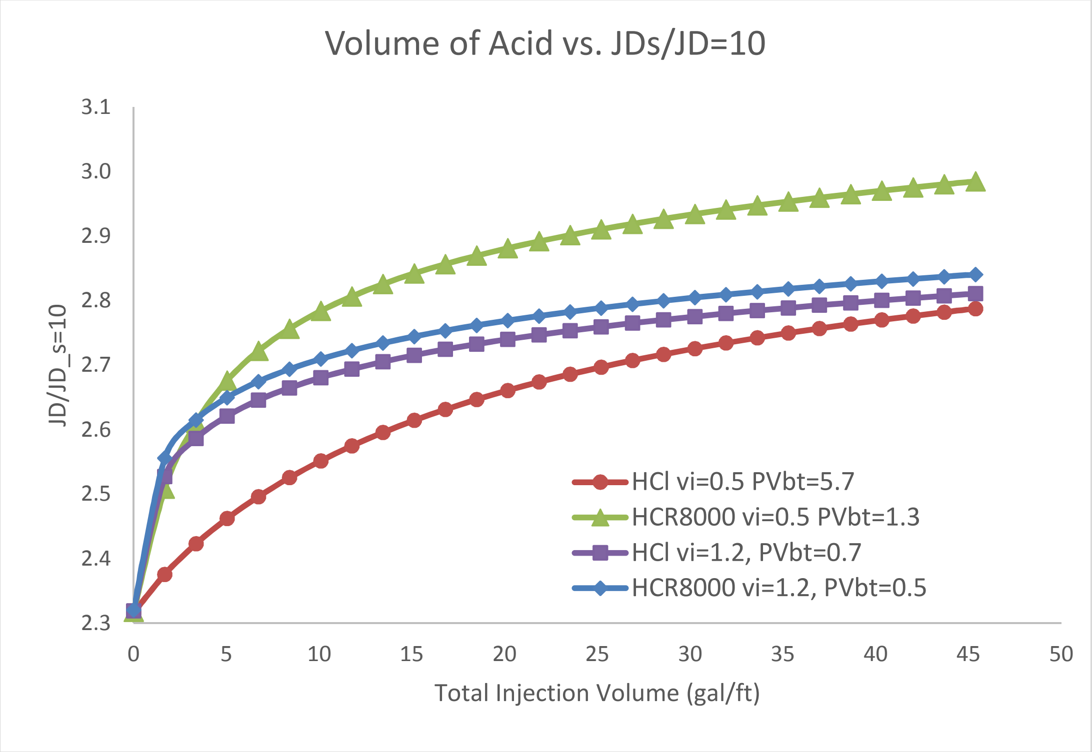

Figure 52. Productivity index comparison at 10 skin HCR-8000

As shown above in the comparisons, HCR-8000 is a more efficient chemical at low interstitial velocity compared to 15% HCl. HCR-8000 maintains higher performance for both interstitial velocity rates selected for comparison. This means that if the acid stimulation operation has a limitation for pumping rate so that the feasible interstitial velocity is below where their curves cross over in Figure 47, HCR-8000 has definite advantage compared to 15% HCl. However, if the interstitial velocity is close to 1.5cm/min or higher, at which the wormhole efficiency curves cross over, 15% HCl becomes more efficient.

4.3 Volumetric Dissolving Power Analysis

The volumetric dissolving power of acids were analyzed in this section. It is an empirical calculation for obtaining acid's dissolving capacity. The volumetric dissolving power equation was obtained from Economides et al. (2012) and is as following:

$$\beta = \frac{\nu_{mineral} MW_{mineral}}{\nu_{acid} MW_{acid}} \ldots\ldots (4.32)$$

β is the gravimetric dissolving power, and Equation 5.13 comes from stoichiometric calculations for the acid dissolution. For 100% HCl and $CaCO_3$,

$$\beta_{100} = \frac{(1)(100.1)}{(2)(36.5)} = 1.37 \frac{lb_m CaCO_3}{lb_m HCl} \ldots\ldots (4.33)$$

From this we can calculate 15% HCl:

$$\beta_{15} = (0.15)\beta_{100} = (0.15) * 1.37 = 0.21\frac{lb_mCaCO_3}{lb_mHCl} \ldots\ldots\ldots\ldots\ldots\ldots\ldots\ldots\ldots\ldots\ldots\ldots(4.34)$$

And subsequently, the volumetric dissolving power χ can be calculated, which is the ratio of the volume of mineral dissolved and volume of acid used.

$$\chi = \beta\frac{\rho_{acid}}{\rho_{mineral}} \ldots\ldots\ldots\ldots\ldots\ldots\ldots\ldots\ldots\ldots\ldots\ldots\ldots\ldots\ldots\ldots\ldots\ldots\ldots\ldots(4.35)$$

So, for 15% HCl, the volumetric dissolving power can be calculated like this:

$$\chi_{15} = 0.21\left(\frac{lb_mCaCO_3}{lb_mHCl}\right)\frac{(1.07)(62.4)(lb_m15\%HCl)(ft^3 15\%HCl)}{169\left(\frac{lb_mCaCO_3}{ft^3CaCO_3}\right)} = 0.082\left(\frac{ft^3CaCO_3}{ft^3 15\%HCl}\right)\ldots\ldots\ldots\ldots\ldots(4.36)$$

Because the data show how much acid was used for each experiment, it is possible to obtain the volumetric dissolving power constants for each of the acids by measuring the dry weights of cores before and after the experiment. The calculated results are shown below in Tables 19 and 20. HCR-6000 volumetric dissolving power was not able to be calculated due to the absence of the cores.

Table 19. HCR-7000 Volumetric Dissolving Power Calculation

	Dry Weight (g)								
HCR-7000	Before Acidizing	After Acidizing	Δ (g)	Vol. Dissolved (cm3)	Injection Rate (ml/min)	(ml/s)	Injection Time (s)	Vol. Acid (ml)	χ (Vol. Rock/Vol. Acid)
IC108	497.4	495.9	1.5	0.554	5	0.083	200	16.7	0.033
IC109	497	495.5	1.5	0.554	2	0.033	600	20.0	0.028
IC111	500.6	498.7	1.9	0.701	10	0.167	128	21.3	0.033
IC112	498.5	497.1	1.4	0.517	3	0.050	335	16.8	0.031
LDA16	499.9	493.6	6.3	2.325	1	0.017	4600	76.7	0.030
									0.031

Table 20. HCR-8000 Volumetric Dissolving Power Calculation

	Dry Weight (g)								
HCR-8000	Before Acidizing	After Acidizing	Δ (g)	Vol. Dissolved (cm3)	Injection Rate (ml/min)	(ml/s)	Injection Time (s)	Vol. Acid (ml)	χ (Vol. Rock/Vol. Acid)
IC101	500.1	498.9	1.2	0.443	2.0	0.033	580	19.3	0.023
IC102	500.5	499.1	1.4	0.517	5.0	0.083	241	20.1	0.026
IC 201	499.2	495.4	3.8	1.402	1.0	0.017	1550	25.8	0.054
IC 202	499.2	497.4	1.8	0.664	0.8	0.013	3350	44.7	0.015
									0.029

Equation 5.17 showed that for 15% HCl, the volumetric dissolving power is 0.082. The HCR-7000 and HCR-8000 volumetric dissolving power values are less than half of 15% HCl, yet the acids themselves provide more efficient wormhole propagation at low interstitial velocity. This consequently leads to a conclusion that the volumetric dissolving power value does not directly correlate with the acid efficiency in matrix acidizing treatment.

5. CONCLUSION AND RECOMMENDATION

In this research, three novel acids systems were studied. The effect of the chemical retardation of reaction on wormhole development and overall skin reduction as well as production improvement was analyzed in detail through core flood matrix acidizing experiments and mathematical simulation of Buijse-Glasbergen model. Based on the results, the following could be concluded:

1. The acid flux curves generated by coreflood experiments show that the chemically reduced reactivity acids have higher efficiency and performance at any flow rates below 15% HCl's optimum interstitial velocity.
2. The Buijse-Glasbergen mathematical modeling shows the acids' performance at lower interstitial velocity results in superior skin reduction, higher productivity index, and deeper wormhole penetration compared to 15% HCl per volume of injected acid.
3. The volumetric dissolving power constant does not directly correlate with the acid efficiency in wormhole propagation.

There exists some limitations for the experimental and simulated work. The experimental work inherently includes possibilities of error. Whether it may be human or mechanical error, it is impossible to eliminate the chances of errors within the results. For simulated analysis, there may be some assumptions that do not reflect reality of the production environment. The assumptions made within Buijse-Glasbergen wormhole propagation model may result in values that are not observed in the field.

Future work can be done with comparing different models of wormhole development to calculate production and skin with these acids. More analysis could also be conducted for chemical dynamics of the acids and how they work in a molecular level to understand the chemical mechanism behind the results. Then, a larger scale coreflood experiment can be conducted to substantiate the experimental and simulated results even further. Also, different types of acids can be compared with these novel acids with regards to their reaction rate and diffusion rate. Because organic acids have similar dissolving power as these acids but have significantly higher pore volume to break through, it would be an interesting study to compare what makes the novel acids so efficient. The study should include chemical molecular dynamics and reaction rate comparison. There can also be case studies for each of the acid systems with industry data for flow rates, rock type, wellbore size, etc. This could determine the most feasible rate at which the particular acid performance is at its maximum. In addition, different rock types could be tested with these acids: sandstone, chalk, dolomite, etc. The experimental procedure would be the same, but the results may differ significantly.

REFERENCES

Buijse, M. A. (1997, January 1). Understanding Wormholing Mechanisms Can Improve Acid Treatments in Carbonate Formations. Society of Petroleum Engineers. doi:10.2118/38166-MS

Buijse, M. A., & Glasbergen, G. (2005, January 1). A Semi-Empirical Model To Calculate Wormhole Growth in Carbonate Acidizing. Society of Petroleum Engineers. doi:10.2118/96892-MS

Chang, F. F., Nasr-El-Din, H. A., Lindvig, T., & Qui, X. W. (2008, January 1). Matrix Acidizing of Carbonate Reservoirs Using Organic Acids and Mixture of HCl and Organic Acids. Society of Petroleum Engineers. doi:10.2118/116601-MS

Cheng, H., Zhu, D., & Hill, A. D. (2017, August 1). The Effect of Evolved CO_2 on Wormhole Propagation in Carbonate Acidizing. Society of Petroleum Engineers. doi:10.2118/178962-PA

Crowe, C. W., McGowan, G. R., & Baranet, S. E. (1990, May 1). Investigation of Retarded Acids Provides Better Understanding of Their Effectiveness and Potential Benefits. Society of Petroleum Engineers. doi:10.2118/18222-PA

Dong, K., Zhu, D., & Hill, A. D. (2017, June 1). Theoretical and Experimental Study on Optimal Injection Rates in Carbonate Acidizing. Society of Petroleum Engineers. doi:10.2118/178961-PA

Dong, Kai (2012). Experimental Investigation for the Effect of the Core Length on the Optimum Acid Flux in Carbonate Acidizing. Master's thesis, Texas A&M University

Economides, M. J., Hill, A. D., Economides, C., & Zhu, D. (2015). Petroleum Production Systems (2nd ed.). Upper Saddle River, NJ: Prentice Hall.

Etten, J., Zhu, D., & Hill, A. D. (2015, June 1). The Combined Effect of Permeability and Pore Structure on Carbonate Matrix Acidizing. Society of Petroleum Engineers. doi:10.2118/174314-MS

Fredd, C. N., & Fogler, H. S. (1999, September 1). Optimum Conditions for Wormhole Formation in Carbonate Porous Media: Influence of Transport and Reaction. Society of Petroleum Engineers. doi:10.2118/56995-PA

Frick, T. (2016). Horos CT Processing Workflow. Department of Petroleum Engineering, Texas A&M University

Ghosh, V. (2013). Matrix Acidizing Parallel Core Flooding Apparatus (Master’s Thesis). Texas A&M University

Grabski, Elizabeth 1985- (2012). Matrix Acidizing Core Flooding Apparatus: Equipment and Procedure Description. Master's thesis, Texas A&M University. Available electronically from http : / /hdl .handle .net /1969 .1 /148417.

Hoefner, M. L., & Fogler, H. S. (1989, February 1). Fluid-Velocity and Reaction-Rate Effects During Carbonate Acidizing: Application of Network Model. Society of Petroleum Engineers. doi:10.2118/15573-PA

Knox, J. A., Pollock, R. W., & Beecroft, W. H. (1965, January 1). The Chemical Retardation of Acid and How it can be Utilized. Petroleum Society of Canada. doi:10.2118/65-01-02

Mahmoud, M. A., & Nasr-El-Din, H. A. (2012, January 1). Modeling of the Flow of Chelating Agents in Porous Media in Carbonate Reservoirs Stimulation. Society of Petroleum Engineers. doi:10.2118/150065-MS

McDuff, D., Shuchart, C. E., Jackson, S., Postl, D., & Brown, J. S. (2010, January 1). Understanding Wormholes in Carbonates: Unprecedented Experimental Scale and 3-D Visualization. Society of Petroleum Engineers. doi:10.2118/134379-MS

McLeod, H. O. (1984, December 1). Matrix Acidizing. Society of Petroleum Engineers. doi:10.2118/13752-PA

Panga, M. K. R., Ziauddin, M., Gandikota, R., & Balakotaiah, V. (2004, January 1). A New Model for Predicting Wormhole Structure and Formation in Acid Stimulation of Carbonates. Society of Petroleum Engineers. doi:10.2118/86517-MS

Shirley, R., Jin X. (2017). Permeability & Acid Flooding Procedure. Harold Vance Department of Petroleum Engineering. Texas A&M University.

Sokhanvarian, K., Pummarapanthu, T., Arslan, E., Nasr-El-Din, H. A., Shimek, N., & Smith, K.

(2017, April 3). A New In-Situ Generated Acid System for Carbonate Dissolution in Sandstone and Carbonate Reservoirs. Society of Petroleum Engineers. doi:10.2118/184506-MS

Zakaria, A. S., Nasr-El-Din, H. A., and Ziauddin, M. 2015. Predicting the Performance of the Acid-Stimulation Treatments in Carbonate Reservoirs With Nondestructive Tracer Tests. *SPE Journal*. SPE-174084-PA (in press; posted February 2015).

Ziauddin M., and Bize, E. 2007. The Effect of Pore-Scale Heterogeneities on Carbonate Stimulation Treatments. Presented at the SPE Middle East Oil and Gas Show and Conference, Kingdom of Bahrain, 11-14 March. SPE-104627-MS.

APPENDIX A

FIGURES

Figure A-1. IC23 Outlet

Figure A-2. IC23 Inlet

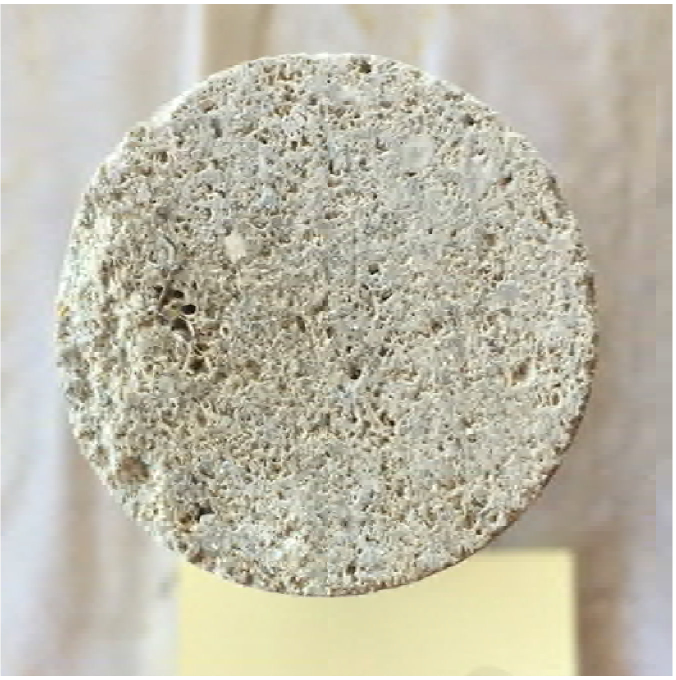

Figure A-3. IC22 Outlet

Figure A-4. IC22 Inlet

Figure A-5. IC21 Outlet

Figure A-6. IC21 Inlet

Figure A-7. IC20 Outlet

Figure A-8. IC20 Inlet

Figure A-9. IC19 Outlet

Figure A-10. IC19 Inlet

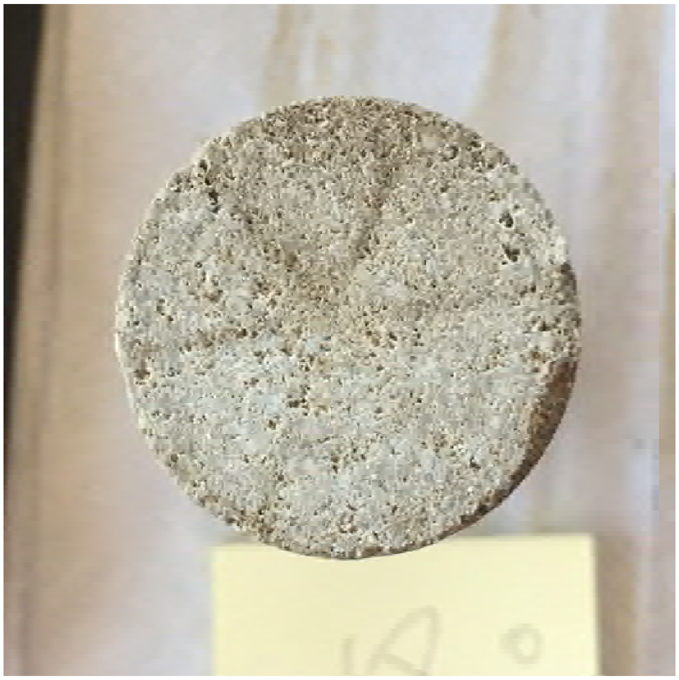

Figure A-11. IC18 Outlet

Figure A-12. IC18 Inlet

Figure A-13. IC16 Outlet

Figure A-14. IC16 Inlet

Figure A-15. IC15 Outlet

Figure A-16. IC15 Inlet

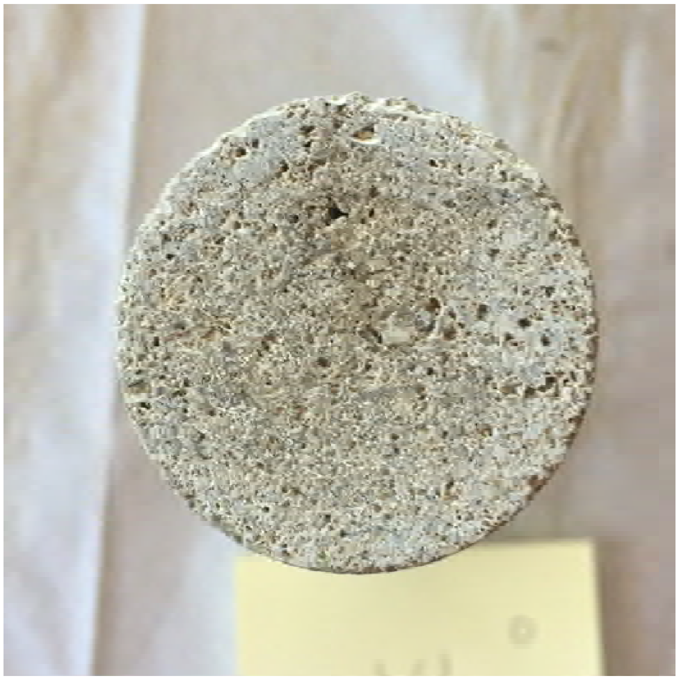

Figure A-17. IC14 Outlet

Figure A-18. IC14 Inlet

Figure A-19. IC13 Outlet

Figure A-20. IC13 Inlet

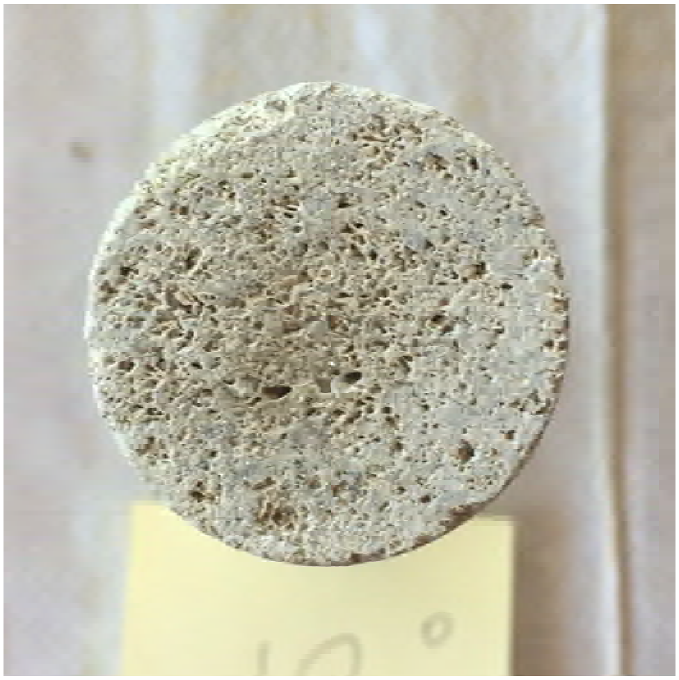

Figure A-21. IC12 Outlet

Figure A-22. IC12 Inlet

Figure A-23. IC11 Outlet

Figure A-24. IC11 Inlet

Figure A-25. IC10 Outlet

Figure A-26. IC10 Inlet

Figure A-27. IC9 Outlet

Figure A-28. IC9 Inlet

Figure A-29. IC6 Outlet

Figure A-30. IC6 Inlet

Figure A-31. IC5 Outlet

Figure A-32. IC5 Inlet

Figure A-33. IC4 Outlet

Figure A-34. IC4 Inlet

Figure A-35. IC3 Outlet

Figure A-36. IC3 Inlet

Figure A-37. IC2 Outlet

Figure A-38. IC2 Inlet

Figure A-39. IC1 Outlet

Figure A-40. IC1 Inlet


Figure A-41. IC101 Inlet


Figure A-42. IC101 Outlet


Figure A-43. IC102 Inlet


Figure A-44. IC102 Outlet

Figure A-45. IC103 Inlet

Figure A-46. IC103 Outlet

Figure A-47. IC104 Inlet

Figure A-48. IC104 Outlet

Figure A-49. IC106 Inlet

Figure A-50. IC106 Outlet

Figure A-51. IC107 Inlet

Figure A-52. IC107 Outlet

Figure A-53. IC108 Inlet

Figure A-54. IC108 Outlet

Figure A-55. IC109 Inlet

Figure A-56. IC109 Outlet

Figure A-57. IC110 Inlet

Figure A-58. IC110 Outlet

Figure A-59. IC111 Inlet

Figure A-60. IC111 Outlet

Figure A-61. IC112 Inlet

Figure A-62. IC112 Outlet

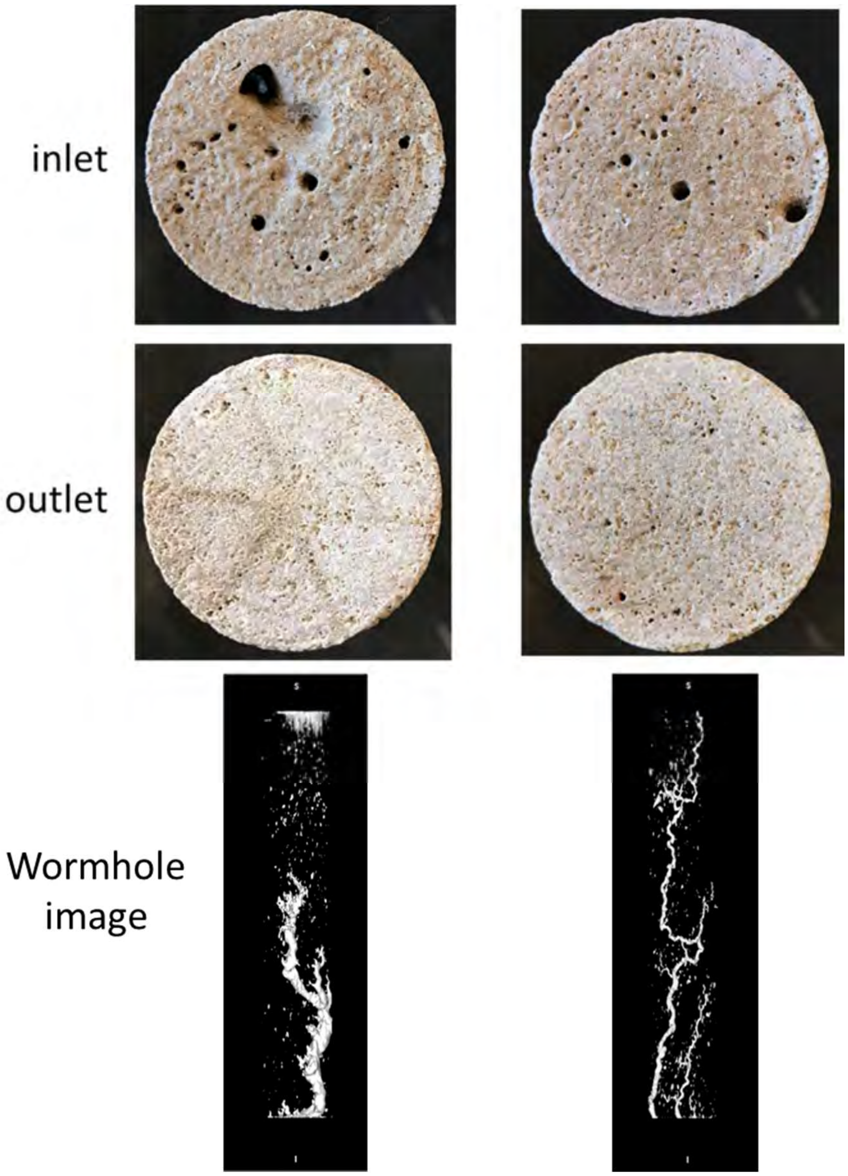

Figure A-63. Testing result for 15%HCl(left) and HCR-6000(right) at 8ml/min

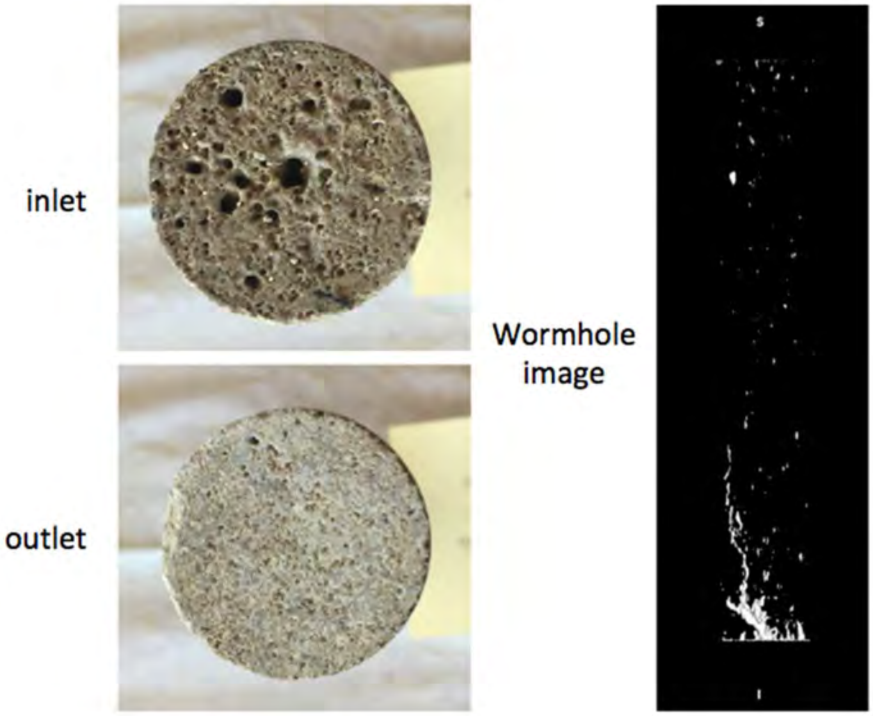

Figure A-64. HCR-6000 result for 0.3ml/min injection rate

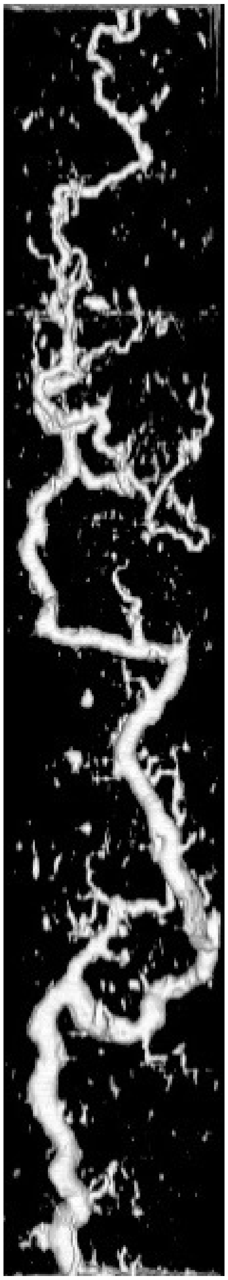

Figure A-65. CT Scan image of LDA16: vi = 0.57 cm/min, PV_{BT} = 2.11

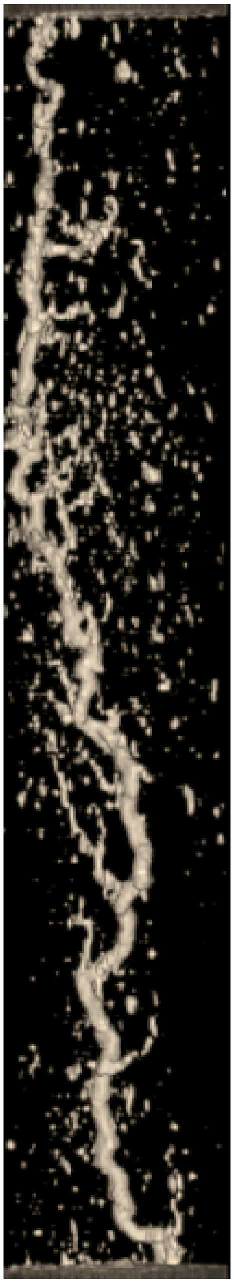

Figure A-66. CT Scan image of IC109: vi = 1.2 cm/min, PV_{BT} = 0.57

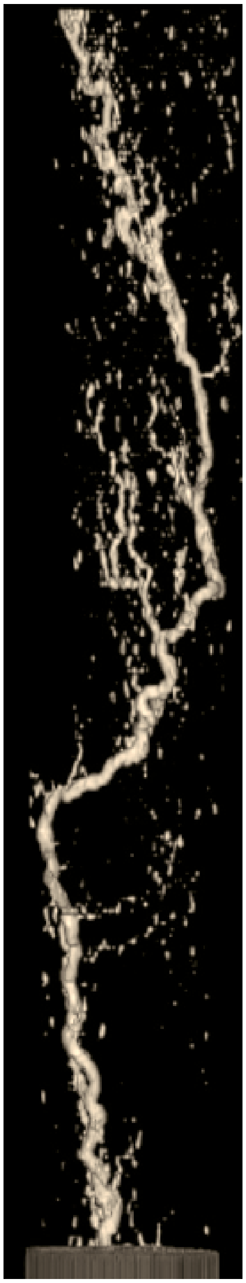

Figure A-67. CT Scan image of IC112: vi = 1.92 cm/min, PV_{BT} = 0.49

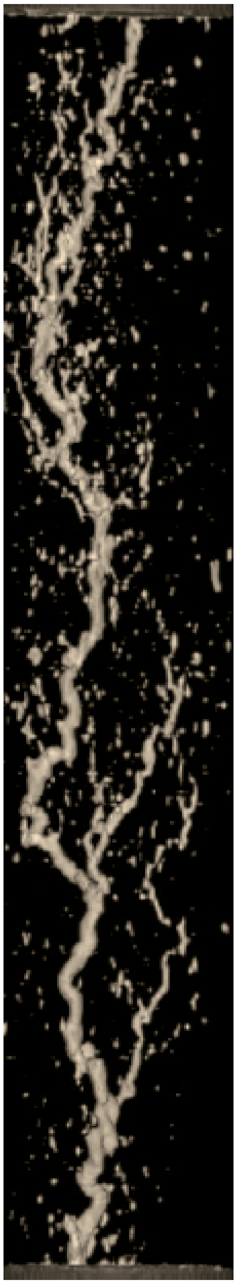

Figure A-68. CT Scan image of IC108: vi = 3.01 cm/min, PV_{BT} = 0.46

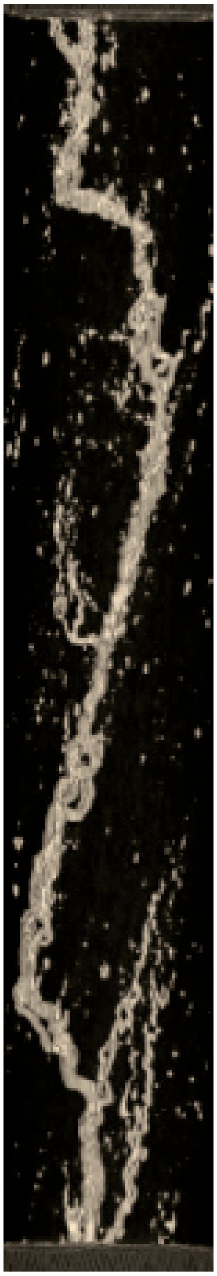

Figure A-69. CT Scan image of IC111: vi = 6.37 cm/min, PV_{BT} = 0.63

Figure A-70. CT Scan image of IC202: vi = 0.50 cm/min, PV_{BT} = 1.34

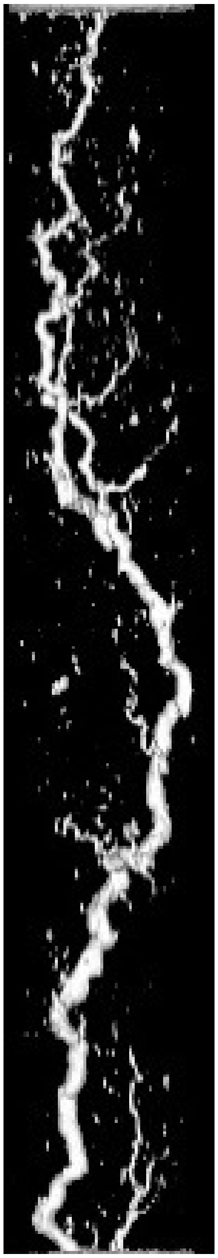

Figure A-71. CT Scan image of IC201: vi = 0.64 cm/min, PV_{BT} = 0.78

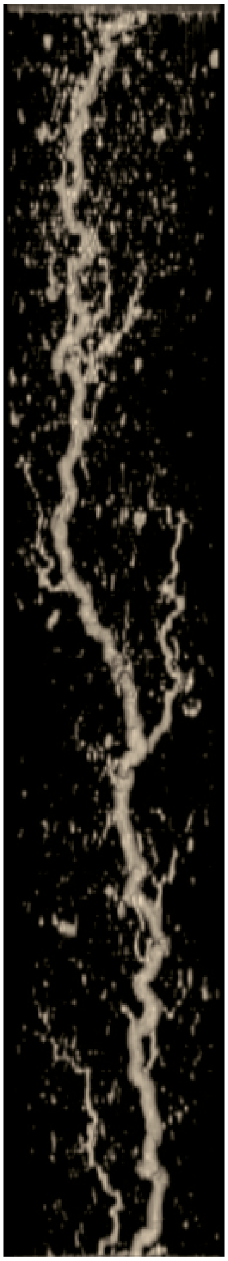

Figure A-72. CT Scan image of IC101: vi = 1.3 cm/min, PV_{BT} = 0.58

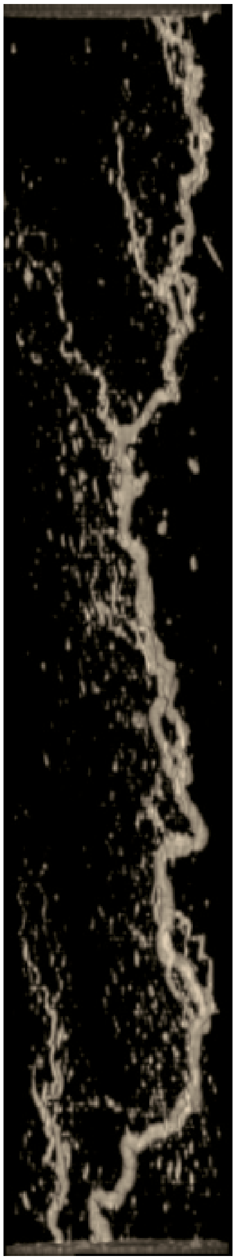

Figure A-73. CT Scan image of IC102: vi = 3.27 cm/min, PV_{BT} = 0.61